On elastic gaps in strain gradient plasticity: 3D discrete dislocation dynamics investigation

Yaovi Armand Amouzou-Adoun, Mohamed Jebahi, Marc Fivel, Samuel Forest, Jean-Sébastien Lecomte, Christophe Schuman, Farid Abed-Meraim

On elastic gaps in strain gradient plasticity: 3D discrete dislocation dynamics investigation

Yaovi Armand AMOUZOU-ADOUN[a], Mohamed JEBAHI[a], Marc FIVEL[b], Samuel FOREST[c], Jean-Sebastien LECOMTE[a], Christophe SCHUMAN[a], Farid ABED-MERAIM[a]

[a]*Arts et Metiers Institute of Technology, CNRS, Université de Lorraine, LEM3, F-57000 Metz, France*
[b]*Univ. Grenoble Alpes, CNRS, Grenoble INP, SIMaP, F-38000 Grenoble, France*
[c]*Mines Paris, PSL University, Centre des matériaux (CMAT), CNRS UMR 7633, BP 87, 91003 Evry, France*

Abstract

Although presenting attractive features in dealing with small-scale size effects, strain gradient plasticity (SGP) theories can lead to uncommon phenomena for some boundary value problems. Almost all non-incremental (Gurtin-type) SGP theories including thermodynamically-consistent higher-order dissipation predict elastic gaps under certain non-proportional loading conditions. An elastic gap is defined as a finite change in the equivalent yield stress after an infinitesimal change in the strain conditions, at the occurrence of the non-proportional loading source. The existence of such gaps in reality is largely questioned and represents a major source of uncertainty preventing the development of robust SGP theories for real small-scale applications. Using 3D discrete dislocation dynamics (3D-DDD), the present paper aims at investigating size effects within micron-scale single crystal structures under various non-proportional loading conditions, including tension-compression-passivation, bending-passivation and tension-bending. An in-depth investigation of the occurrence of elastic gaps under these conditions, which are known to entail such gaps when using classical non-incremental SGP theories, is conducted. The obtained 3D-DDD results reproduce well known experimentally confirmed size effects like Hall-Petch effect, Asaro's type III kinematic hardening and reversible plasticity. However, no evidence of the phenomenon of elastic gaps is found, which constitutes a first indication that this phenomenon may not exist in reality. The simulations are performed on face-centered cubic (FCC) Nickel single grains with cuboid shapes ranging from $2\,\mu\mathrm{m}$ to $15\,\mu\mathrm{m}$ and different orientations.τ

Keywords: Discrete dislocation dynamics, Non-proportional loading conditions, Passivation, Size effects, Elastic gaps, Strain gradient plasticity

1. Introduction

With the exponential trend towards miniaturization, micron-sized products have become widely used in various high technology fields, such as microelectronics and microbotics. As shown by several small-scale experiments [1, 2, 3, 4, 5, 6], in the size range between hundreds of nanometers and few tens of micrometers, the strength of metallic materials is no longer scale-independent and the peculiar phenomenon "smaller is stronger" appears. Influence of size effects must then be carefully considered to design accurate small-scale components. Pioneered by Aifantis [7], strain gradient plasticity (SGP) presents very promising capabilities to capture such effects. This theory has received a strong scientific interest in the last three decades and numerous SGP models have been developed for single- and poly-crystal structures [8, 9, 10, 11, 12, 13, 14, 15].

Email addresses: yaovi.amouzou-adoun@ensam.eu (Yaovi Armand AMOUZOU-ADOUN), mohamed.jebahi@ensam.eu (Mohamed JEBAHI)

According to Hutchinson [9], two classes of SGP theories can be distinguished: (i) incremental theories, in which the higher-order stresses are calculated incrementally as a function of the increments of plastic strains and their gradients, and (ii) non-incremental (also called Gurtin-type) theories, in which the higher-order stresses are themselves related to the increments of the plastic strains and their gradients. Although providing interesting results in terms of prediction of size effects, the earliest incremental SGP models developed in the literature [16] do not always satisfy the requirement of nonnegative dissipation [17, 18]. To circumvent this issue, modified incremental models, in which the higher-order stresses are assumed to be purely energetic, have been developed [9, 19, 20]. However, these models cannot consider thermodynamically-consistent higher-order dissipation, which is necessary at small scales according to some authors [21, 22]. Until now, there exists no accepted recipe for incremental SGP models formulation including thermodynamically-consistent higher-order dissipation [19]. To overcome this limitation, non-incremental SGP models have been developed [8, 13, 18, 23]. As formulated, these models always satisfy the requirement of nonnegative dissipation, making them the most commonly used in the literature. However, as pointed out by several authors [9, 13, 19, 24], they may lead to uncommon effects for some boundary value problems, such as the occurrence of elastic gaps under non-proportional loading conditions.

Initially reported by Fleck et al. [24], the phenomenon of elastic gaps under non-proportional loading conditions can be defined as an interruption of the initiated plastic flow after an infinitesimal change in the boundary conditions until the mechanical state (evolving elastically) reaches a new yield point. An illustration of this phenomenon is given by Fleck et al. [24] using a 2D sample subjected to two types of non-proportional loading conditions: tension followed by passivation and tension followed by bending. As stated by Fleck et al. [19], almost all non-incremental SGP theories including thermodynamically-consistent higher-order dissipation lead to elastic gaps under certain loading conditions. However, this phenomenon has never been observed elsewhere, neither experimentally nor numerically using other small scale methods [12, 15, 19]. Its physical reality is highly questioned and represents a source of uncertainty, preventing the development of robust SGP models capable of correctly predicting the size-dependent behavior of materials. In the absence of works studying these gaps from a physical point of view, the scientific investment on SGP theories has reached a bifurcation point making the community divided into those who consider elastic gaps as "unknown" size effects (then possibly physical) and those who see no physical reasons for their occurrence in reality (as they reflect an instantaneous increase of the apparent yield surface). Therefore, investigation of such gaps and their existence in reality are highly required. In the lack of experimental techniques allowing for applying non-proportional loading conditions at the scale of interest, small-scale numerical approaches can reasonably provide a good alternative to conduct such an investigation. Among these approaches, 3D discrete dislocation dynamics (3D-DDD) emerges as a powerful physics-based numerical tool that can be applied to perform accurate micron-scale simulations at affordable cost [25, 26, 27]. One of the main objectives of the present paper is to address for the first time the problematic of the elastic gaps using this approach, as suggested by several authors [19, 28].

Starting to be developed in the late 1990s, 3D-DDD aims at giving full details of the plasticity mechanisms based on dislocation activity. It can provide an accurate description of small scale plasticity with relatively few modeling assumptions. This approach intrinsically includes an internal length scale via the Burgers vector associated with the dislocation lines and can naturally reproduce challenging size effects. It has been widely used to investigate experimentally observed size effects within face-centered cubic (FCC) and body-centered cubic (BCC) crystals under uniaxial loading conditions [29, 30, 31, 32], with the emphasis often put on the size-dependence of the flow stress. The associated results have allowed for predicting accurately the well-known Hall-Petch (HP) effect [1, 2]. Hussein et al. [33] have applied this approach to study different cross-slip mechanisms identified from atomistic simulations of FCC crystals. The obtained results are in agreement with experimental observations, which shows the effectiveness of the applied approach to reproduce challenging small scale mechanisms of plastic deformation. 3D-DDD has also widely been applied to simulate micro-bending of thin foils [34, 35, 36, 37, 38] and micro-torsion of thin wires

[30, 39], which naturally produce strain gradient effects. The phenomenon of dislocation pile-up around the neutral axis of a beam in bending or at the center of a micropillar in torsion has clearly been evidenced, in a way matching experimental results. Ryu et al. [30] have demonstrated that 3D-DDD is able to reproduce the strong reversible plasticity observed in the cyclic torsion experiments [40]. This phenomenon has also been noticed in experimental single crystal bending works [41, 42, 43]. Other 3D-DDD simulations involving cyclic loading conditions to study kinematic effects can be found in the literature [30, 35, 44]. However, these works have mainly focused on classical Bauschinger effects. The type III kinematic hardening (KIII) of Asaro [45], which is the subject of extensive on-going SGP discussions [13, 28, 46, 47, 48, 49], has not been studied yet using realistic 3D-DDD simulations.

Although proportional loading conditions are widely used in 3D-DDD simulations, only few works involving non-proportional ones can be found in the literature [50, 51]. 2D-DDD has been used in [50] to study the response of a plate under combined tension-bending. More recently, Gravell and Ryu [51] have studied the flow stress evolution at the nano-scale in the presence of combined tension-torsion. No dislocation-based works studying the phenomenon of elastic gaps under non-proportional loading conditions exist in the literature. The present paper aims at providing 3D-DDD in-depth investigation of size effects under different proportional and non-proportional loading conditions, with a focus on the issue of elastic gaps for the first time. Both free and passivated surface conditions are considered and three types of non-proportional loading conditions are involved: tension-compression-passivation, tension-bending, and bending-passivation. The latter conditions are known to yield elastic gaps when using classical non-incremental SGP theories. Cyclic loading conditions are also applied to discuss phenomena like Asaro's type III kinematic hardening and reversible plasticity during unloading.

After the present introduction, the paper is structured as follows. Section 2 presents an illustration of the elastic gap phenomenon and introduces a description of the 3D-DDD methodology and the associated modeling assumptions. Section 3 deals with size effects under proportional and non-proportional tension-compression loading conditions. The proportional and non-proportional bending loading conditions are the subject of section 4. Finally, a summary is presented in section 5.

2. Methodology and modeling assumptions

As previously mentioned, one of the main objectives of this paper is to investigate the challenging issue of elastic gaps, which is commonly encountered in the context of Gurtin-type strain gradient plasticity theories. The term "elastic gap" was introduced by [24] to describe an unusual absence or interruption of any plastic activity beyond the classical yield point until a new yield stress is reached. Based on [19], two types of elastic gaps can be distinguished (see Fig. 1 for illustration): (i) elastic gap at initial yield, which can be described as a delay in the plastic flow at the classical yield point, and (ii) elastic gap after an infinitesimal change in the boundary conditions, which causes an interruption of the initiated plastic flow until a further yield point is reached. The first type of elastic gaps is somewhat accepted in the literature [13, 28, 49] and is typically explained by the strengthening effect, *i.e.*, increase of the apparent yield stress with decreasing size, which has been observed in many small scale experiments [4, 52, 53]. It is worth mentioning that the strengthening effect, as observed experimentally, is more likely associated with a micro-plastic regime with a high hardening rate at the beginning of plasticity, rather than a delay in the plastic flow in the strict sense as predicted by SGP theories. The latter type of elastic gaps has never been observed experimentally or numerically using small scale models. The present work focuses on this type of elastic gaps using 3D-DDD.

The 3D-DDD simulations are performed using the code TRIDIS which has been developed by Fivel et al. [54, 55, 56]. Face-centred cubic (FCC) Nickel single grains are used in the simulations, with the material parameters listed in Tab. 1. The dislocation lines are discretized into successions of pure screw and edge segments embedded in an elastic medium. They are able to glide on the $\frac{1}{2}\langle 110\rangle\{111\}$ slip systems with the

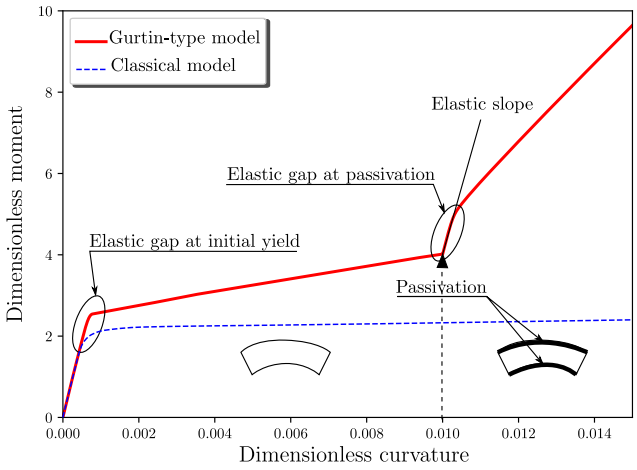

Fig. 1. Illustration of elastic gaps obtained with a Gurtin-type SGP model for a 2D plate submitted to bending with free surface followed by passivation of top and bottom edges and continued bending.

possibility to create junctions or to be annihilated according to local interaction rules [55]. Every portion of the dislocation lines moves under the effect of the Peach-Koehler force [57]. To avoid dynamic effects (out of scope of the present work), the 3D-DDD simulations are performed under quasi-static conditions, *i.e.*, the loading rate is chosen sufficiently low to let dislocations reach an equilibrium position during the entire simulation. Each dislocation moves at a velocity v calculated by a linear mobility law given by:

$$v = \frac{\tau_{\text{eff}}}{B} b \tag{1}$$

with b the magnitude of the Burgers vector, B the phonon drag coefficient and τ_{eff} the effective resolved shear stress. The latter variable is defined by:

$$\begin{cases} \tau_{\text{eff}} = \Big(|\tau^*| - \tau_{\text{Peierls}} \Big)^+ \text{sign}(\tau^*) \\ \tau^* = \left[\left(\dfrac{1}{b} [\hat{\boldsymbol{\sigma}} + \tilde{\boldsymbol{\sigma}}] \mathbf{b} \right) \times \mathbf{l} \right] \cdot \mathbf{g} + \tau_{\text{lt}} \end{cases} \tag{2}$$

where $\big(\bullet \big)^+$ denotes the positive part of $\bullet$, $\mathbf{l}$ is the line vector of the considered segment, $\mathbf{g}$ is the glide direction vector, τ_{lt} is the line tension which accounts for the local curvature of a dislocation, $\hat{\boldsymbol{\sigma}}$ is the applied stress, $\tilde{\boldsymbol{\sigma}}$ is the internal stress generated by the dislocation network in an infinite medium as formulated by Cai et al. [58] and τ_{Peierls} represents the lattice friction which acts as a source of resistance to dislocation motion. In this work, τ_{Peierls} is fixed to be of the same order of magnitude as the one associated with copper (FCC crystal) [27, 51]. For simplicity, image forces are neglected in the present 3D-DDD simulations. Based on [59], these forces have no significant influence at micron scale. Therefore, the applied stress $\hat{\boldsymbol{\sigma}}$ is homogeneous in the case of tension-compression and varying linearly through the thickness in the case of bending [26]. The total stress at a given point in the studied domain is given by the superposition of the applied and internal stresses $\boldsymbol{\sigma} = \hat{\boldsymbol{\sigma}} + \tilde{\boldsymbol{\sigma}}$, as illustrated in Fig. 2a. Following the same reasoning, the displacement at a given point in the studied domain $\mathbf{u}$ is decomposed into dislocation plastic contribution $\tilde{\mathbf{u}}$ and correction term $\hat{\mathbf{u}}$.

Concerning the preparation of the DDD numerical samples, following several works from the literature [29, 33, 38, 61], the initial dislocation network for all the simulations consists of random Frank-Read sources (FRs). An example of an initial 3D-DDD configuration is presented in Fig. 2b. The FRs initial lengths (L_{FRs}) are ranging between $\frac{d}{4}$ and $\frac{d}{3}$, with $d = \sqrt[3]{V}$ and V the volume of the studied domain. This gives an average

Tab. 1. Nickel parameters inspired by the literature [33, 60].

Shear modulus μ (MPa)	Poisson ratio ν	Burgers vector magnitude b (Å)	Friction stress τ_{Peierls} (MPa)	Activation volume V_{act} (Å^3)	τ_{III} (MPa)	Drag coefficient B (Pa.s)
75200	0.376	2.489	37.6	$20b^3$	77	1.1×10^{-5}

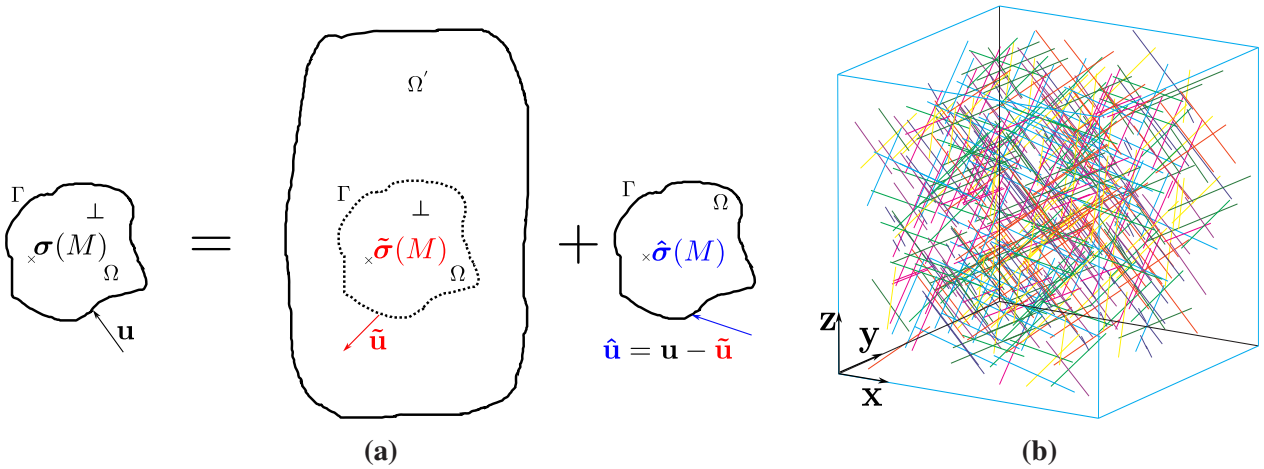

Fig. 2. Methodology of the simulations: **(a)** the superposition method; **(b)** example of initial dislocation network of a grain with initial dislocation density $\rho_0 = 60 \times 10^{11}$ m^{-2}.

source length of around $0.3\,d$, which is in the order of the average stable source length [62]. It is worth mentioning that other procedures can be found in the literature to generate DDD numerical samples. One of them is the relaxation procedure proposed in [31]. Although providing more realistic initial dislocation networks, this procedure is time-consuming and leads to qualitatively similar results compared to those obtained with random FRs (see Appendix A), which explains the choice of the latter procedure in the present work. Inspired by [63], to reduce computation time, the FRs are only generated on the active slip systems with the same number of sources on each system. For each dislocation segment created with a positive sign, an opposite one with the same length L_{FRs} is automatically added somewhere in the grain so that the initial total Nye tensor vanishes. Different grain orientations with respect to the loading directions are used to cover different cases of activated single-, double- or multi-slip configurations, which are required to better understand some key mechanisms of size effects. Finally, to alleviate statistical effects on the results, three DDD samples with randomly distributed FRs sources are constructed for each case study and the arithmetic average of the associated macroscopic responses is taken as the final result.

In TRIDIS, the cross-slip mechanisms are modeled using the probabilistic model of Verdier et al. [55], in which the cross-slip probability is determined by:

$$P = \beta \frac{l}{l_0} \frac{\Delta t}{t_0} \exp\left(\frac{\tau_{\text{dev}} - \tau_{\text{III}}}{kT} V_{\text{act}}\right) \tag{3}$$

where β is a scaling factor to ensure $P \in [0, 1]$, l is the screw-segment length, l_0 is the reference length, τ_{dev} is the resolved effective shear stress in the deviate plane, τ_{III} is the resolved shear stress at the onset of stage III, V_{act} is the activation volume, k is the Boltzmann constant and T is the absolute temperature. Although widely used in 3D-DDD simulations [31, 37], this model is relatively simple and only provides an approximate description of the cross-slip mechanisms. Furthermore, some associated parameters (*e.g.*, β

and l_0) are generally numerically chosen without physical background. To avoid biased conclusions about important results that can be caused by this model, a comparative study between results obtained with and without activating cross-slip mechanisms has been carried out. An example of the comparison results is given in Appendix B. It has been found that activation of such mechanisms does not conceptually modify the results. Simulations with more realistic description of cross-slipping using the atomistic-based model developed by Longsworth and Fivel [64] will be made in a future work.

3. 3D-DDD simulations of tension-compression

This section aims at providing an enhanced understanding of size effects under tension-compression loading conditions. Proportional cyclic conditions are applied to enrich the discussions on the kinematic hardening effects, particularly Asaro's type III kinematic hardening [45]. Then, non-proportional cyclic conditions are applied to investigate the issue of elastic gaps. For all the simulations, cubic grains having $< 100 >$ orientations are considered, with the tension-compression loading applied in $\mathbf{z} = [001]$ direction. This leads to multi-slip configuration, whose Schmid factors are summarized in Tab. 2. To ensure quasi-static conditions, the tension loading is applied such that the strain rate is around $\dot{\varepsilon}_{33} = 300\,\mathrm{s}^{-1}$, with a time step $\Delta t \approx 10^{-10}\,\mathrm{s}$. It was verified that when the strain rate is divided by three, no significant dynamic effects are observed in the 3D-DDD results. The rate $\dot{\varepsilon}_{33} = 300\,\mathrm{s}^{-1}$ is then applied for computational efficiency reasons.

3.1. Proportional tension-compression case

Several works have reported on tension and tension-compression 3D-DDD simulations to study small scale phenomena like Hall-Petch relation and Bauschinger effects [29, 31, 63, 65]. With the aim of extending these works, the present subsection focuses on the Asaro's type III kinematic hardening. To this end, a complete cycle of tension-compression loading is applied on the considered grains, with the grain boundaries assumed to be passivated (*i.e.*, impenetrable to dislocations) during the entire simulation.

Fig. 3a presents the macroscopic tension-compression response, in terms of stress as a function of the total strain in the loading direction, for a grain with side $d = 5\,\mu\mathrm{m}$ and initial dislocation density $\rho_0 = 3 \times 10^{11}\,\mathrm{m}^{-2}$. This figure shows the domination of kinematic hardening with respect to isotropic hardening. The so-called reversible plasticity or also anomalous Bauschinger effect, with reverse plastic flow already occurring when the overall stress is still under unloading (*i.e.*, before it is reversed), is also clearly observed. A significant amount of recoverable plastic strain $\varepsilon_{\mathrm{rp}}$ is evidenced in Fig. 3a. This phenomenon has been reported in several experimental works [40, 52]. The obtained Bauschinger and reversible plasticity effects can be explained by the dislocation patterns accumulated at the passivated grain boundaries. Another important result from Fig. 3a is the uncommon non-convex shape of the cyclic response, with inflection points. Although not commented by the authors, similar non-convex shape has been obtained by Jiang et al. [66] using 3D-DDD. This shape can be identified with the type III kinematic hardening of Asaro [45], corresponding to a first-in/last-out sequence of dislocation motion. It represents the most perfect form of recovery of plastic memory. The obtained non-linear behavior with inflection points has already been observed experimentally in some materials, as illustrated in Fig. 3b taken from [67] for Fe-Cr alloy. 3D-DDD makes it possible to reproduce such a behavior in a quite natural manner, which is very useful for the SGP community. Indeed, it has recently been shown that SGP approaches based on non-quadratic defect energy forms can provide an accurate continuum description of this behavior [10, 13, 28, 46, 49, 68]. 3D-DDD simulations can then be helpful to select the right defect energy form, as well as to identify the associated parameters, for a given material.

Effects of the initial dislocation density ρ_0 are examined in Fig. 4a, where only plastic strains are considered for clarity. The non-linear kinematic behavior with inflection points becomes less marked with increasing ρ_0. The case of $\rho_0 = 60 \times 10^{11}\,\mathrm{m}^{-2}$ corresponds to nearly classical behavior with Bauschinger

Tab. 2. Schmid factors m_s associated with tension-compression simulations (loading direction $\mathbf{z} = [001]$). Schmid-Boas notation is used for the slip systems.

Slip system	B4	D4	D1	C1	B5	C5	D6	A6	A2	B2	C3	A3
$m_s^{\mathbf{z}=[001]}$	**0.41**	**-0.41**	**-0.41**	**0.41**	0.	0.	0.	0.	**-0.41**	**0.41**	**0.41**	**-0.41**

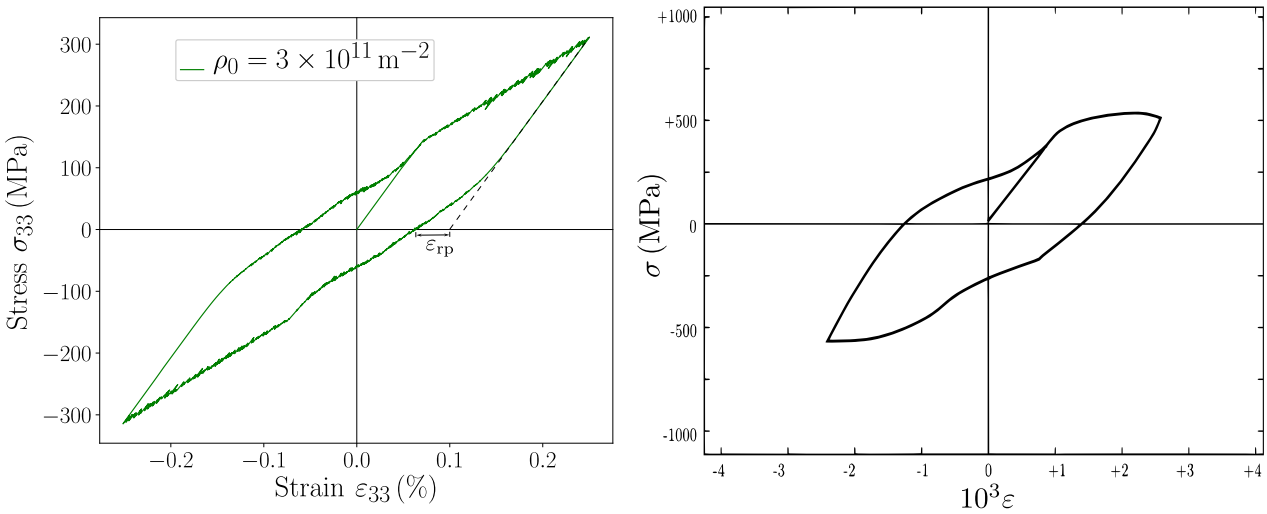

(a) **(b)**

Fig. 3. Macroscopic tension-compression response: **(a)** 3D-DDD result obtained using a grain with side $d = 5\,\mu\mathrm{m}$ and initial dislocation density $\rho_0 = 3 \times 10^{11}\,\mathrm{m}^{-2}$ ($\varepsilon_{\mathrm{rp}}$ denotes the recoverable plastic strain); **(b)** experimental result obtained using large-grained Fe-Cr alloy aged at 923 K for 72 h (reproduced from [67]).

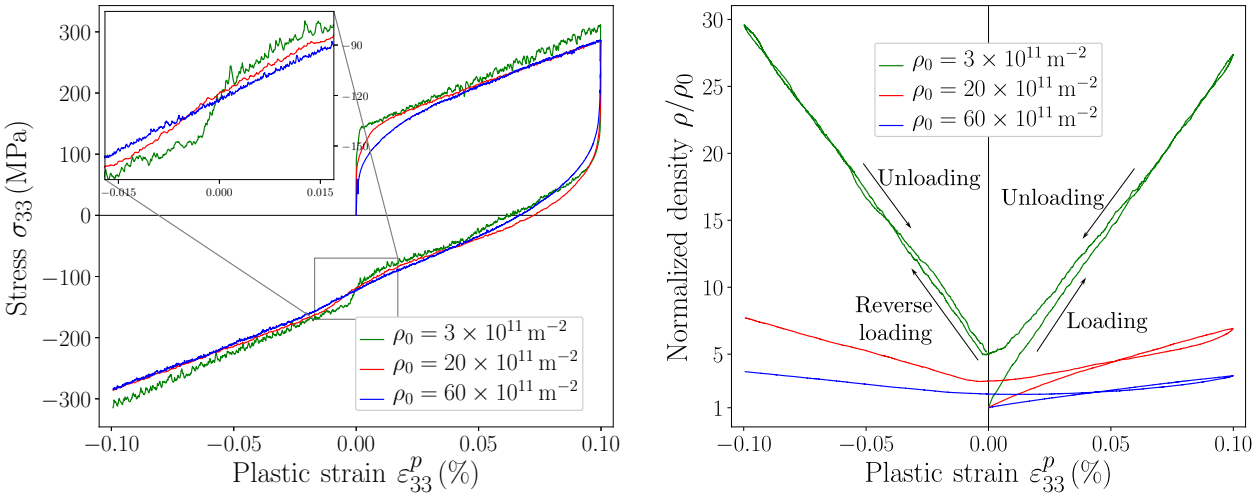

(a) **(b)**

Fig. 4. Initial dislocation density effects in a grain with size $d = 5\,\mu\mathrm{m}$: **(a)** tension-compression responses for different ρ_0; **(b)** evolution of the normalized dislocation density during the loading cycle.

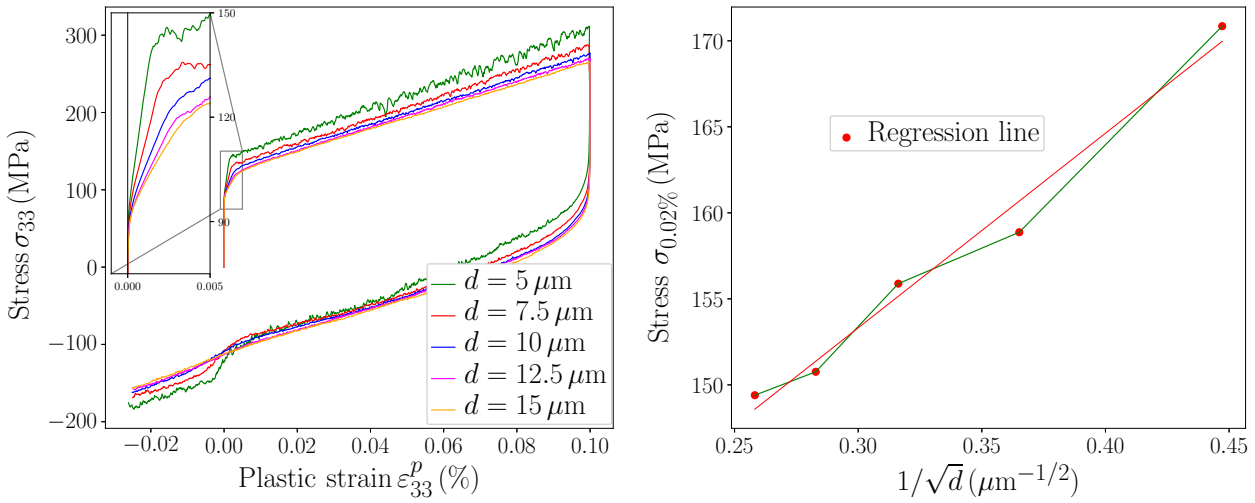

(a) **(b)**

Fig. 5. Effects of the grain size d in the case of multi-slip configuration: **(a)** tension-compression responses for various values of d; **(b)** evolution of the apparent yield stress measured at 0.02% plastic strain as function of $1/\sqrt{d}$.

effects as observed at the macroscopic scale. This result may explain the disappearance of the inflection points in the experiments of Taillard et Pineau [67] after a high number of loading cycles. As shown in Fig. 4b, the dislocation density increases after each loading cycle, reducing the non-linear effects in the next one. Using a large value of ρ_0, the latter effects disappear, which explains their absence at the macroscopic scale. Still on the effects of ρ_0, it can also be shown from Fig. 4a that the flow stress decreases with increasing ρ_0. Although contradicting the classical Taylor relation, this result is echoed in the generalized version of this relation given by [29]:

$$\tau/\mu = \frac{\beta_T}{d\sqrt{\rho}} + \alpha_T b\sqrt{\rho} \tag{4}$$

with β_T and α_T material dimensionless constants. This generalized version predicts a decrease of the flow stress with the dislocation density until a certain level, after which the flow stress takes a more classical evolution as stipulated by the classical Taylor relation (second term of (4)) due to high forest dislocation effects. Unfortunately, in the case of large (several microns) grains, it is extremely costly to use dislocation densities large enough to obtain directly the classical Taylor evolution [29].

Investigation of the grain size effects on the cyclic tension-compression response is presented in Fig. 5, obtained using the same initial dislocation density $\rho_0 = 3 \times 10^{11}\,\text{m}^{-2}$. As seen in the zoomed-in region in Fig. 5a, an initial steep-sloped plastic evolution occurs immediately after the conventional yielding before the plastic slope significantly decreases at a further yield stress. This latter stress can be interpreted as an apparent yield stress, beyond which the plastic deformation is considerably activated. As depicted in Fig. 5a, the apparent yield stress increases with decreasing the grain size d, which is in accordance with the strengthening effect observed in numerous small scale experiments [52, 53]. Moreover, linear regression analysis indicates that the apparent yield stress evolves approximately linearly with $d^{-1/2}$ as predicted by the Hall-Petch (HP) relation (Fig. 5b). It should be noted that the value of the HP exponent is subject to discussions in some experimental works [60, 69], due to technical difficulties encountered in measuring it. In the present case involving cubic single crystals, the value of $-1/2$ was found to be a close fitting value. Regarding effects of d on the Asaro's kinematic hardening, Fig. 5a shows that this behavior becomes more

marked with decreasing d. On the contrary, nearly classical linear kinematic hardening behavior is obtained in the case of large grain size, confirming the absence of the inflection points at the macroscopic scale.

3.2. Non-proportional tension-compression-passivation case

In the present subsection, non-proportional tension-compression-passivation simulations are carried out to investigate the issue of elastic gaps. These simulations consist of two-step loading. During the first step, tension loading in $\mathbf{z} = [001]$ direction is applied with free grain boundaries to dislocations (free surface boundary conditions), *i.e.*, dislocations can freely leave the cubic grain through all its 6 faces. Then, after a certain level of accumulated plastic strain $\varepsilon_{33}^{p,\text{pass}}$, the grain boundaries are passivated (passivated surface boundary conditions) before pursuing the tension loading. No further modification of the passivation conditions occurs until the end of the loading cycle.

Fig. 6a presents the associated stress-plastic-strain responses obtained using two values of passivation plastic strain $\varepsilon_{33}^{p,\text{pass}}$ within a grain having a side $d = 5\,\mu\text{m}$ and initial dislocation density $\rho_0 = 3 \times 10^{11}\,\text{m}^{-2}$. For comparison purposes, proportional responses obtained assuming free and passivated surface conditions during the entire simulation are also presented in this figure. Using proportional loading with free surfaces, nearly flat response is obtained after yielding (red curve in Fig. 6a). Since dislocations can freely leave the crystal through the outer surfaces of the simulated box, no significant hardening effect is observed. On the contrary, the proportional case with passivated surfaces exhibits large strain hardening effects (green curve in Fig. 6a) due to the phenomenon of dislocations piling-up at the grain boundaries as previously discussed in subsection 3.1. Focusing on the non-proportional responses (Fig. 6a), before passivation, the obtained stress-plastic-strain curves are identical to those associated with the case of proportional tension-compression with free surface conditions. The occurrence of passivation during the plastic regime only modifies the hardening slope without interrupting the plastic flow, regardless of the value of the passivation plastic strain $\varepsilon_{33}^{p,\text{pass}}$ at which the grain surfaces are passivated. In other words, no elastic gap is obtained at the occurrence of the non-proportional loading source. The dislocations inside the grain are still able to continue creating enough plastic strain to accommodate the applied loading. The strain hardening rate after passivation is identical to that obtained using passivated surfaces from the beginning of the simulation.

The obtained non-proportional results with no elastic gaps contradict the predictions of classical non-incremental (Gurtin-type) SGP theories, which are the most commonly used in the literature. When including thermodynamically-consistent higher-order dissipation, these models predict an elastic gap at the occurrence of passivation (*i.e.*, interruption of the plastic flow until a new yield point). In the results of Fleck et al. [24], the magnitude of the elastic gap depends on the size of the specimen h (or equivalently the internal length scale l). On the contrary, the absence of elastic gaps in the present 3D-DDD simulations is not limited to a particular grain size d or a given initial dislocation density ρ_0, as shown in Fig. 6b and Fig. 6c. It should be noted that the modified Gurtin-type model proposed in [13] allows for overcoming the issue of elastic gaps under tension-passivation. However, this model cannot avoid elastic gaps under any non-proportional loading conditions, especially under conditions leading to gradient effects prior to the occurrence of the non-proportional loading source (*e.g.*, non-proportional bending-passivation conditions which are discussed in the next section). To the authors knowledge, only two SGP models allowing for considering thermodynamically-consistent higher-order dissipation while systematically avoiding elastic gaps exist in the literature [12, 15]. However, these models substantially deviate from classical Gurtin-type approaches. The present 3D-DDD results suggest that these two recent models would provide a better continuum description of small scale plasticity with respect to classical Gurtin-type SGP models.

Analyzing the tension-compression curves under the entire loading cycle (Fig. 6a), the non-linear kinematic hardening with inflection points is observed in all the cases implying passivation, which introduces the possibility of dislocations piling-up at the grain boundaries. The value of the passivation plastic strain $\varepsilon_{33}^{p,\text{pass}}$ influences the position of the inflection points which occur at approximately the same plastic strain value reached under reverse loading. This can be explained by the fact that the inflection phenomenon occurs at

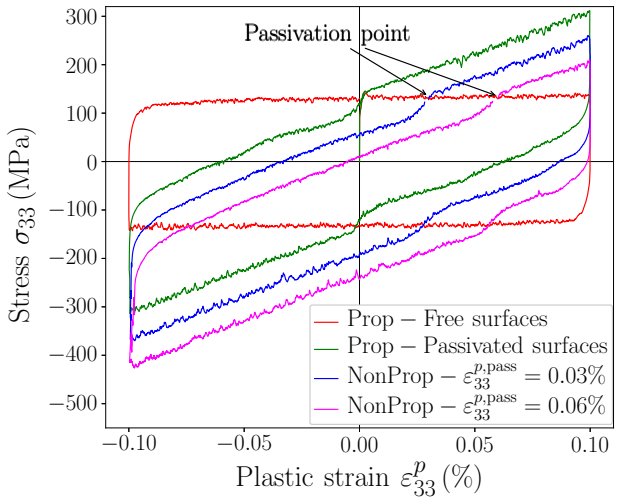

(a)

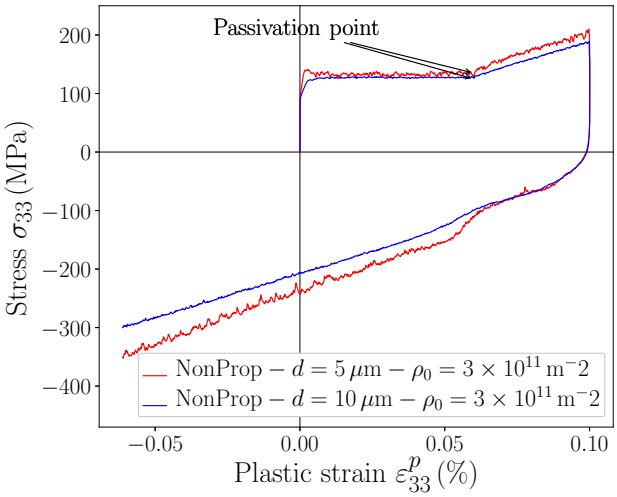

(b)

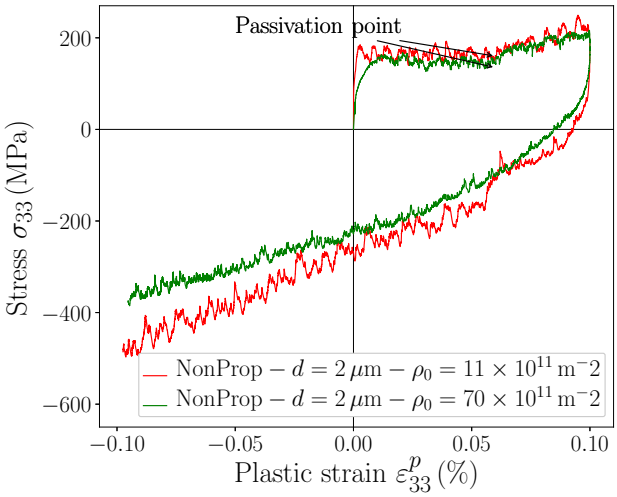

(c)

Fig. 6. Investigation of the occurrence of elastic gaps: **(a)** comparison between proportional and non-proportional tension-compression results for $d = 5\,\mu$m and $\rho_0 = 3 \times 10^{11}\,\text{m}^{-2}$; **(b)** effect of the grain size d on the non-proportional tension-compression response; **(c)** effect of the initial dislocation density ρ_0 on the non-proportional tension-compression response.

Tab. 3. Schmid factors for two grain orientations: multi-slip ($\mathbf{x} = [100];\ \mathbf{y} = [010]; \mathbf{z} = [001]$) and double slip ($\mathbf{x} = [\bar{1}12];\ \mathbf{y} = [1\bar{1}1]; \mathbf{z} = [110]$) cases.

Slip system	B4	D4	D1	C1	B5	C5	D6	A6	A2	B2	C3	A3
$m_{\mathrm{s}}^{\mathbf{x}=[100]}$	**-0.41**	**0.41**	0.	0.	**0.41**	**-0.41**	**0.41**	**-0.41**	0.	0.	**-0.41**	**0.41**
$m_{\mathrm{s}}^{\mathbf{x}=[\bar{1}12]}$	**0.41**	0.	0.	**0.41**	-0.27	-0.27	0.	0.	-0.27	0.14	0.14	-0.27

the vanishing of the gradient effects, *i.e.*, at the end of the dislocations unpiling-up, where the dislocation network goes back to its initial configuration at the beginning of the process of piling-up (at the occurrence of passivation).

4. 3D-DDD simulations of plastic bending

Size effects in bending have been studied in several works using 2D-DDD [36, 50, 70] and 3D-DDD [35, 37, 38, 71], while only free surface boundary conditions are generally involved. To enhance these works, proportional bending conditions with free and passivated grain surfaces are first considered. Then, non-proportional bending conditions, including bending-passivation and tension-bending, are implied to better investigate the occurrence of elastic gaps when the non-proportional loading source is preceded by the development of gradient effects.

Fig. 7a presents an example of the 3D-DDD numerical samples employed in the bending simulations. 3D beams of volume $V = L \times w \times h = d^3$ and ratio $3:1:1$ are considered, where L, w and h are respectively the length in $\mathbf{x}$ direction, the width in $\mathbf{y}$ direction and the thickness in $\mathbf{z}$ direction. Using the procedure described in [26], the bending loading is applied around the $\mathbf{y}$ axis by imposing linear applied stress $\hat{\sigma}_{11}$ along the thickness, with the neutral plane located at $z = 0$ (left part of Fig. 7b). At each time step ($\Delta t = 2 \times 10^{-11}$ s), the increment of maximum stress (*i.e.*, the stress applied on the top surface) is $\Delta\hat{\sigma}_{11}^{\max} = 4 \times 10^{-2}\,\mathrm{MPa}$, which is very small compared to the friction stress $\tau_{\mathrm{Peierls}} = 37.6\,\mathrm{MPa}$. As explained earlier, it was verified that this level of stress increment does not lead to significant dynamic effects in the 3D-DDD results. Two grain orientations are considered: orientation with $\mathbf{x} = [100]$, $\mathbf{y} = [010]$ and $\mathbf{z} = [001]$ leading to multi-slip configuration and orientation with $\mathbf{x} = [\bar{1}12]$, $\mathbf{y} = [1\bar{1}1]$ and $\mathbf{z} = [110]$ leading to double-slip configuration. The associated Schmid factors are summarized in Tab. 3.

The post-treatment of the bending moment $\mathcal{M}$ and the curvature κ is realized based on the sketch in the right part of Fig. 7b. At a given x, the effective moment $\mathcal{M}(x)$ is calculated by numerical trapezoid integration of the relation:

$$\mathcal{M}(x) = w\int_{-\frac{h}{2}}^{\frac{h}{2}} z\sigma_{11}(x,z)\mathrm{dz} = w\int_{-\frac{h}{2}}^{\frac{h}{2}} z\left[\tilde{\sigma}_{11} + \hat{\sigma}_{11}\right]\mathrm{dz} = w\int_{-\frac{h}{2}}^{\frac{h}{2}} z\left[\tilde{\sigma}_{11} + \frac{z}{h/2}\hat{\sigma}_{11}^{\max}\right](x,z)\mathrm{dz} \quad (5)$$

with $\hat{\sigma}_{11}^{\max}$ the applied stress at the top surface $z = h/2$. Due to the discrete nature of 3D-DDD, the value of the overall moment $\mathcal{M}$ is determined by averaging $\mathcal{M}(x)$ along $\mathbf{x}$ direction. Based on the superposition method (Fig. 2a), the material curvature κ is decomposed into elastic and plastic parts $\kappa = \kappa_e + \kappa_p$ and is evaluated as the average on the two outer vertical surfaces $x = \pm L/2$. Plastic curvature κ_p is determined through the relation $\tilde{u}_1 = \kappa_p xz$, where the plastic contribution $\tilde{u}_1$ is calculated with the formulas proposed by Barnett [72] and implemented in TRIDIS [56]. Elastic curvature is in the same way related to $\hat{u}_1$ using the expression $\hat{u}_1 = \kappa_e xz$. The total curvature is then evaluated by:

$$\kappa(x = \pm L/2) = \frac{2}{L}\left[\left\langle\frac{\tilde{u}_1}{z}\right\rangle_{x=\pm L/2} + \left\langle\frac{\hat{u}_1}{z}\right\rangle_{x=\pm L/2}\right] \quad (6)$$

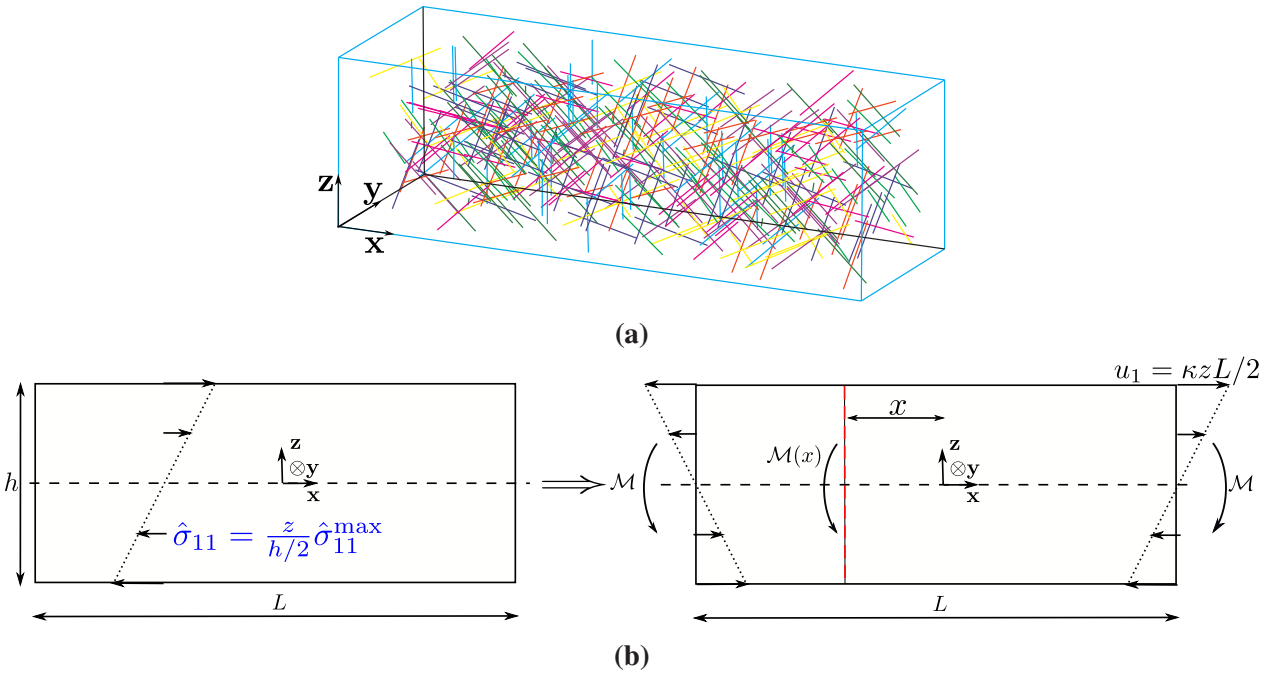

Fig. 7. Bending set-up: **(a)** example of 3D-DDD numerical samples for bending simulations; **(b)** applied stress for bending loading and post-treatment procedure.

where $\left\langle \bullet \right\rangle_{x=a}$ is the mean value of $\bullet$ at $x = a$.

4.1. Proportional bending case

In this subsection, monotonic bending loading is first applied to discuss the "yield point" phenomenon reported by Read [73] using 2D analytical analysis. Then, cyclic bending loading is introduced to study kinematic hardening effects in bending. To simplify the analysis of the results, only double-slip beams are involved in the present subsection (Tab. 3). However, the associated comments and conclusions are also valid for multi-slip configurations as shown in Appendix C.

4.1.1. Monotonic bending loading

Depending on the ratio between the stress required to move dislocations σ_0 and the stress required to create dislocations σ_c ($\alpha = \sigma_0/\sigma_c$), Read [73] has analytically demonstrated that the bending curve of a beam with free surfaces can show softening-like effect (Fig. 8). A 3D-DDD investigation of this effect, which is called "yield point" phenomenon, is proposed hereafter. In the context of 3D-DDD, α can be approximated by $\alpha_{\mathrm{DDD}} = \tau_{\mathrm{Peierls}}/\tau_{\mathrm{ac}}$, where τ_{Peierls} is the friction stress and τ_{ac} is the stress necessary to operate a source. Based on [62], the later stress can be taken equal to the single arm stress:

$$\tau_{\mathrm{ac}} = \tau_{\mathrm{Peierls}} + \eta\mu b\sqrt{\rho} + \frac{k\mu b}{\lambda} \tag{7}$$

where η and k are dimensionless constants and λ is the average stable source length (taken in this work as the average FRs length: $\lambda \approx \left\langle L_{\mathrm{FRs}} \right\rangle$). Consequently, α_{DDD} can be assessed at the beginning of plasticity as ($\rho \approx \rho_0$):

$$\alpha_{\mathrm{DDD}} \approx \left(1 + \eta\frac{\mu b}{\tau_{\mathrm{Peierls}}}\sqrt{\rho_0} + \frac{k\mu b}{\tau_{\mathrm{Peierls}}\left\langle L_{\mathrm{FRs}} \right\rangle}\right)^{-1} \tag{8}$$

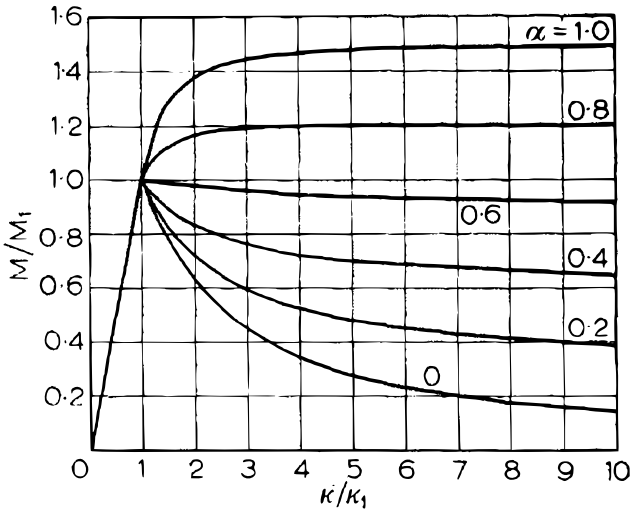

Fig. 8. Illustration of the "yield point" phenomenon in bending (reproduced from [73]).

Given the material parameters, α_{DDD} can be varied either by ρ_0 or by L_{FRs}. It is obvious that, when ρ_0 increases, α_{DDD} decreases, and inversely, when L_{FRs} increases, α_{DDD} increases. Effects of varying α_{DDD} using these two ways are presented in Fig. 9, which is obtained considering a beam with dimensions $L \times w \times h = 9 \times 3 \times 3\,\mu\mathrm{m}^3$ and free surface conditions. As shown in Fig. 9a, in the range of the applied ρ_0, the yield moment and the slope of the moment curve after yielding decrease with increasing ρ_0 (*i.e.,* with increasing the number of FRs). This is in accordance with the generalized Taylor relation given by (4), as explained in subsection 3.1. For $\rho_0 = 100 \times 10^{11}\,\mathrm{m}^{-2}$, the "yield point" phenomenon is significantly noticeable. Using the same value of $\rho_0 = 100 \times 10^{11}\,\mathrm{m}^{-2}$, Fig. 9b shows that the apparent softening in bending can be suppressed by adopting larger FRs, as expected from (8).

The σ_{11} stress distributions along the thickness at two bending stages (designated by 1 and 2 in Fig. 9a) are presented in Fig. 10, for a beam having $L \times w \times h = 9 \times 3 \times 3\,\mu\mathrm{m}^3$ and $\rho_0 = 60 \times 10^{11}\,\mathrm{m}^{-2}$. Due to anti-symmetry of the distributions, only the upper half of the studied beam is considered in the following analysis. The σ_{11} stress profile obtained at stage 1 (blue curve in Fig. 10a) with a plastic region confined between two elastic ones is in good agreement with the analytical profile predicted by Read [73] for a material having $\alpha < 1$. The elastic response in Fig. 10a corresponds to the case with no dislocations. No plastic deformation occurs until σ_{11} at the top surface reaches $\sigma_{11} = \sigma_c$. Then, dislocations are created at this surface and rapidly move inward to the point where $\sigma_{11} = \sigma_0$. Therefore, three regions appear: elastic region $(\mathbf{A})$ extending from the neutral axis to the point where $\sigma_{11} = \sigma_0$ with no moving dislocations, plastic region $(\mathbf{B})$ where $\sigma_{11} = \sigma_0$ with high dislocation density and another elastic region $(\mathbf{C})$ depleted of dislocations due to high σ_{11} stress ($\sigma_{11} > \sigma_0$). As the loading progresses, region $(\mathbf{B})$ increases with respect to region $(\mathbf{A})$ until the two regions merge to obtain a fully plastic central zone with relaxed σ_{11} stress ($\sigma_{11} = \tilde{\sigma}_{11} + \hat{\sigma}_{11} = 0$), as represented by the red curve of Fig. 10a taken at stage 2.

Following the previous analysis made in the case of free surfaces, a comparison with passivated surfaces is drawn. Fig. 11 displays the effect of passivation on the moment-curvature response for different ρ_0. When fixing the initial dislocation density ρ_0, the apparent initial yield stress is higher with passivated surfaces than with free surfaces. This shows that 3D-DDD can also capture the strengthening effect in bending which is more pronounced than in tension case. In addition, larger strain hardening rates are obtained using passivated surface conditions. These results are in accordance with those obtained under tension-compression loading conditions, as discussed in section 3.1. The case of $\rho_0 = 100 \times 10^{11}\,\mathrm{m}^{-2}$, which leads to "yield point" with free surface conditions, reveals a positive work hardening in case of passivation. The difference between free and passivated surface conditions can be understood by observing the stress distribution in the passivation

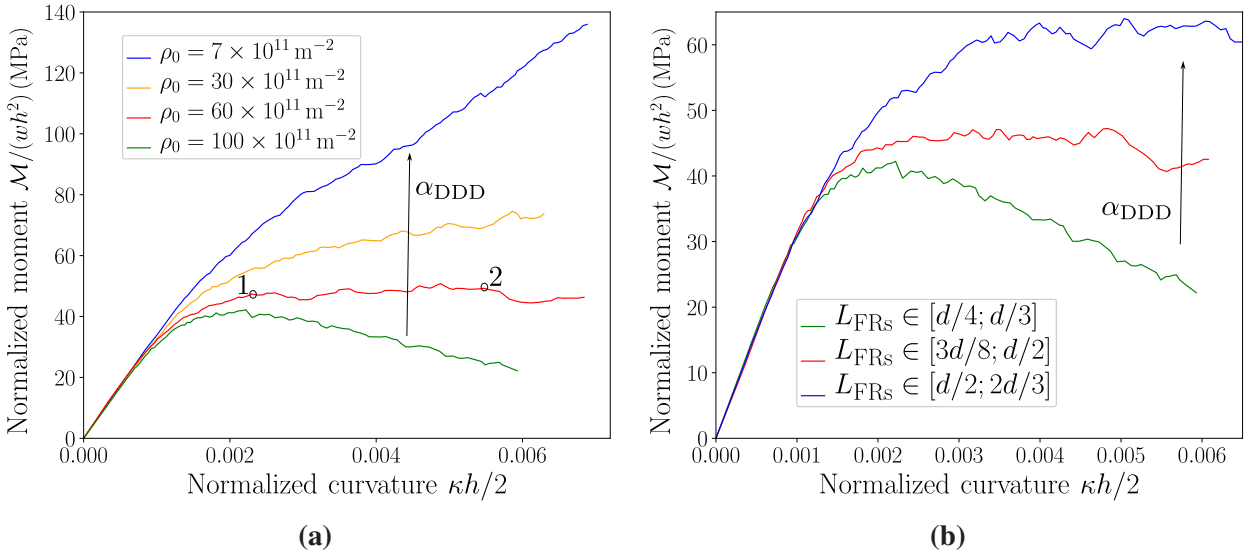

Fig. 9. Investigation of the "yield point" phenomenon: **(a)** effect of the initial dislocation density ρ_0 for $L_{\mathrm{FRs}} \in [d/4; d/3]$ (two points 1 and 2 are indicated for exploitation in Fig. 10); **(b)** effect of the FRs lengths L_{FRs} for $\rho_0 = 100 \times 10^{11}\,\mathrm{m}^{-2}$.

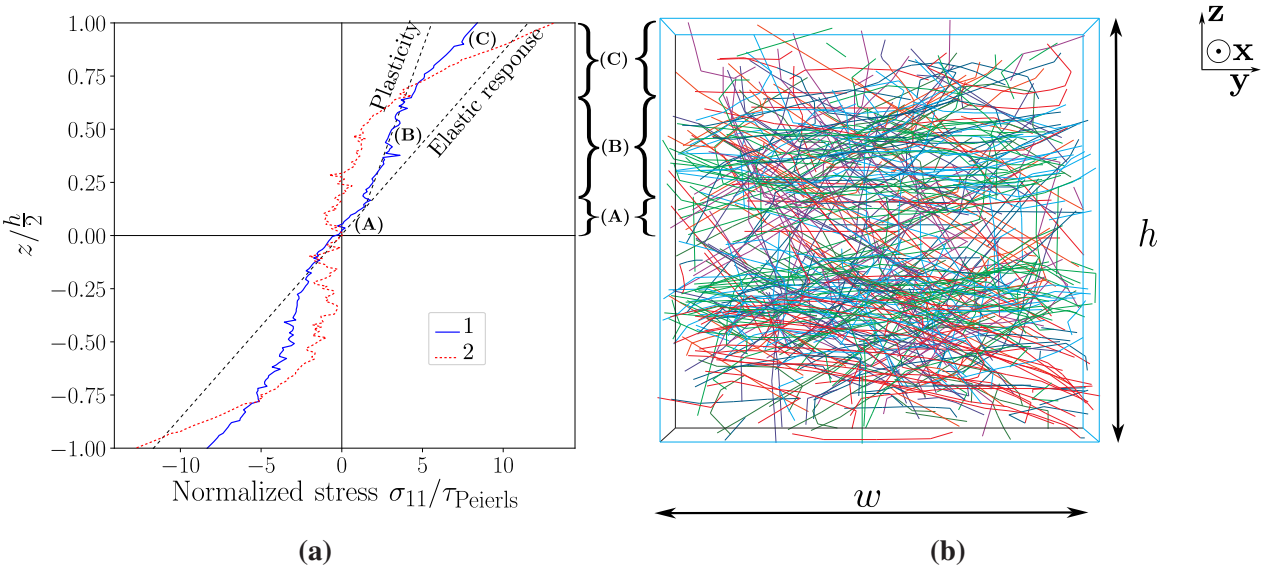

Fig. 10. Evolution of σ_{11} stress in a beam with free surfaces, $L \times w \times h = 9 \times 3 \times 3\,\mu\mathrm{m}^3$ and $\rho_0 = 60 \times 10^{11}\,\mathrm{m}^{-2}$: **(a)** σ_{11} stress profiles at stages 1 and 2 given in Fig. 9a; **(b)** dislocation arrangement in the beam at stage 1.

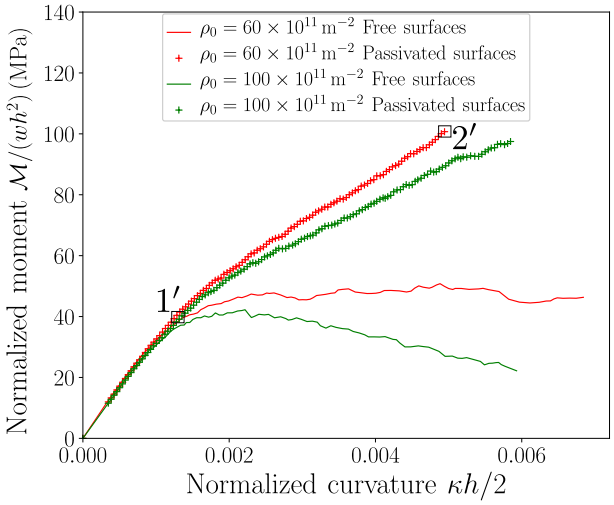

Fig. 11. Bending responses obtained with free and passivated surfaces for different initial dislocation density ρ_0 and $L \times w \times h = 9 \times 3 \times 3\,\mu\mathrm{m}^3$ (two points $1'$ and $2'$ are indicated for exploitation in Fig. 12).

case. Fig. 12a details the stress profiles inside the beam at stage $1'$ (around yielding) and $2'$ (large curvature) from Fig. 11. The dislocation arrangement associated with stage $2'$ is presented in Fig. 12b. It is clear that with passivation, four regions in the studied beam can be distinguished. Besides the three previously discussed regions **(A)**, **(B)** and **(C)**, a region **(D)** appears in the vicinity of the passivated surface as a consequence of dislocation pile-up against this surface. This dislocation pile-up is more compacted than the one at the neutral axis since the stress is much higher in this region. In contrast to free surface conditions at high curvature, regions **(A)** and **(B)** barely merge with passivation conditions. This demonstrates the difficulty of dislocation pile-up to reach the neutral plane resulting from the latter conditions.

In addition to the above discussion on the "yield point" phenomenon, Fig. 13 presents the grain size effects at a constant initial dislocation density $\rho_0 = 60 \times 10^{11}\,\mathrm{m}^{-2}$ with free and passivated surface conditions. The "smaller is stronger" effect is observed using both types of surface conditions, with the apparent yield stress and work hardening increasing with decreasing grain size h. The strengthening effect at initial yielding is also evident.

4.1.2. Cyclic bending loading

To study kinematic hardening effects in bending, a complete bending cycle is considered with both free and passivated surface conditions. Fig. 14 presents the associated results obtained using a beam with dimensions $L \times w \times h = 9 \times 3 \times 3\,\mu\mathrm{m}^3$ and initial dislocation density $\rho_0 = 60 \times 10^{11}\,\mathrm{m}^{-2}$. Relatively low Bauschinger effects are observed using free surface conditions, which allow dislocations to glide out of the beam. On the contrary, using passivated surfaces, strong Bauschinger and non-linear kinematic hardening effects are obtained. The large amount of elastic energy stored in the dislocation pile-ups during loading promotes reverse plasticity during unloading. Furthermore, the reversible plasticity phenomenon, with nonzero recoverable plastic curvature κ_{rp} at zero moment $\mathcal{M}$, is visible. This phenomenon is already experimentally observed in cyclic bending by several authors [41, 42, 43]. Note that κ_{rp} increases with increasing the maximum bending load. Evolution of the dislocation density during the bending cycle is given in Fig. 14b, for free and passivated surfaces. The elastic part during unloading is correlated with a nearly constant dislocation density (plateau-shaped parts of the curves in Fig. 14b). When reverse plasticity starts, the total dislocation density drops, corresponding to the annihilation of dislocation pile-ups created during the loading. It is worth mentioning that the dislocation motion is not completely reversible and the dislocation density after a loading cycle does not correspond to the initial one. Interestingly, it is found that the dislocation density at the end of

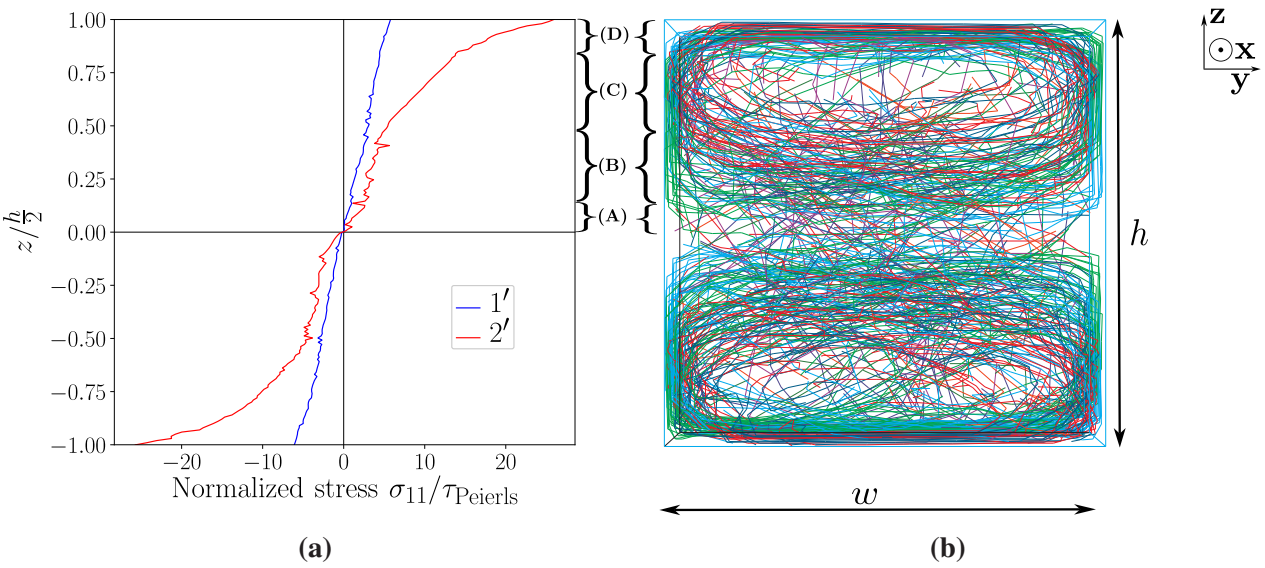

Fig. 12. Evolution of σ_{11} stress in a beam with passivated surfaces, $L \times w \times h = 9 \times 3 \times 3\,\mu\text{m}^3$ and $\rho_0 = 60 \times 10^{11}\,\text{m}^{-2}$: **(a)** σ_{11} stress profiles at stages $1'$ and $2'$ given in Fig. 11; **(b)** dislocation arrangement in the beam at stage $2'$.

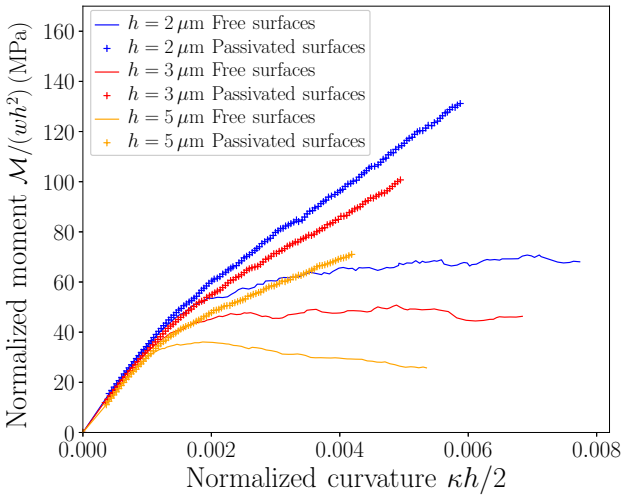

Fig. 13. Size effects with free and passivated surface conditions for initial dislocation density $\rho_0 = 60 \times 10^{11}\,\text{m}^{-2}$.

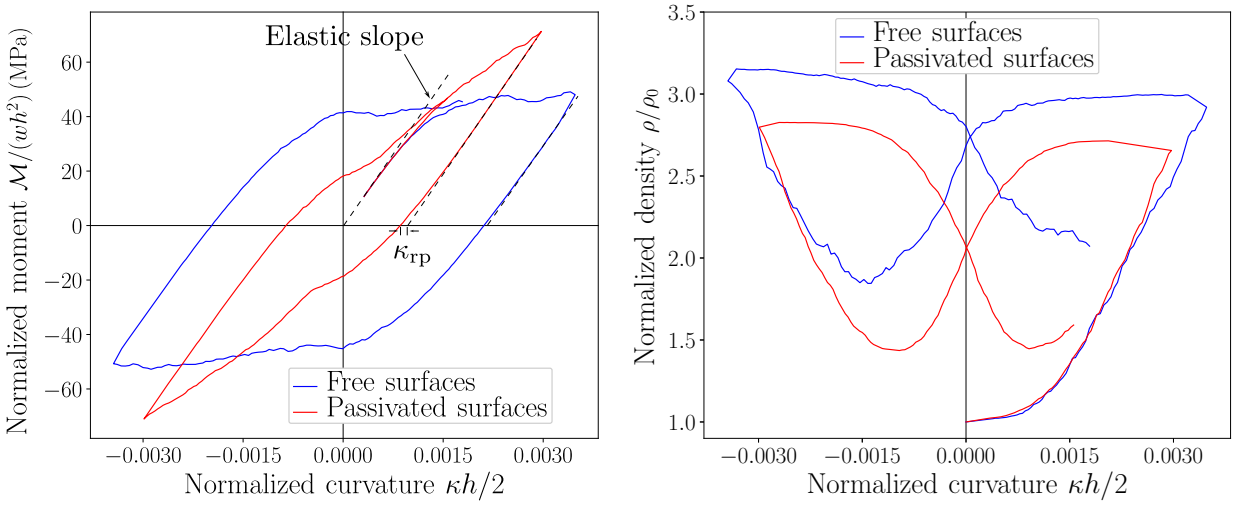

Fig. 14. Comparison between free and passivated surface conditions with $\rho_0 = 60 \times 10^{11}\ \mathrm{m}^{-2}$ and $L \times w \times h = 9 \times 3 \times 3\,\mu\mathrm{m}^3$: **(a)** moment-curvature responses (κ_{rp} is the recoverable plastic curvature); **(b)** evolution of the normalized density during the loading cycle.

loading is larger when using free surfaces than when using passivated ones. Although allowing dislocations to leave the studied beam, free surface conditions allow for creation of much more dislocations in the beam, yielding larger dislocation density.

4.2. Non-proportional bending case: bending-passivation and tension-bending simulations

In this subsection, elastic gaps are investigated in the bending case. To do so, two types of non-proportional bending conditions are implied. The first one (which is referred to hereafter as bending-passivation) consists in applying the same procedure as in tension-compression-passivation, with the tension before passivation replaced by bending. Bending loading is applied with free surfaces until a given amount of plastic curvature, then passivation is applied before continuing the loading cycle. The difference with tension-compression-passivation is the natural presence of dislocation pile-ups at the neutral plane before passivation. The second non-proportional loading is the tension-bending. It is an another complex loading type consisting of two parts: a tension part until a significant amount of accumulated plastic strain in the beam and a bending part while maintaining the reached tension level.

4.2.1. Bending-passivation

The case of non-proportional bending-passivation is discussed in the following. Fig. 15 shows the bending-passivation responses for two orientations (double- and multi-slip configurations) of a beam with dimensions $L \times w \times h = 9 \times 3 \times 3\,\mu\mathrm{m}^3$ and initial dislocation density $\rho_0 = 60 \times 10^{11}\ \mathrm{m}^{-2}$. The multi-slip response is presented in Fig. 15a and the double-slip response in Fig. 15b. In both cases, passivation only increases the work hardening slope without interrupting the plastic flow, *i.e.*, with no occurrence of an elastic slope gap. As shown in Fig. 15, the hardening slope after passivation is quite different from the elastic slope. This result confirms the absence of elastic gaps as in the case of tension-compression-passivation. To verify that the post-passivation response does not depend on the simulation inputs, Fig. 16 presents the results with other values of grain size, initial dislocation density and FRs lengths. For all cases, the post-passivation slope is still distinct from the elastic one, which suggests that elastic gaps may not have physical background in the

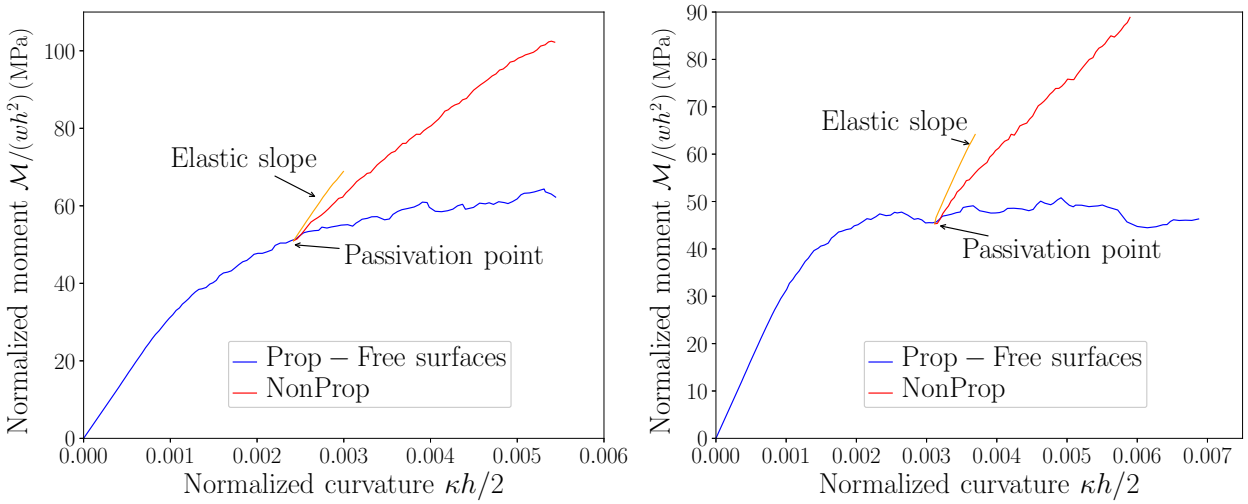

Fig. 15. Bending-passivation responses with $\rho_0 = 60 \times 10^{11}\,\mathrm{m}^{-2}$ and $L \times w \times h = 9 \times 3 \times 3\,\mu\mathrm{m}^3$: **(a)** multi-slip configuration; **(b)** double-slip configuration.

present situation. It is worth noting that the SGP models used in [11, 13] bring out elastic gaps for bending-passivation. The present results encourage the development of gap-free SGP models capable of considering thermodynamically-consistent higher-order dissipation.

4.2.2. Bending after tension: tension-bending

The case of non-proportional tension-bending is considered hereafter. For simplicity, only the case of double-slip is used (see the third line of table 3). Prior to bending, a tension loading is applied until the plastic strain in the loading direction reaches $\varepsilon^p_{11} = 0.1\,\%$. Then, without tension unloading, bending loading is applied. Here, the surfaces are passivated from the beginning of the simulation. The bending part response is compared with the response obtained under proportional bending from the beginning (Fig. 17). The bending slope obtained after an initial tension (without unloading) is identical to that obtained after yielding under proportional bending. This confirms the absence of any trace of elastic gaps.

5. Conclusion

In this work, 3D discrete dislocation dynamics (3D-DDD) was applied to provide an in-depth investigation of size effects under proportional and non-proportional loading conditions in Nickel single grains having different orientations. A particular focus was given to the existence of elastic gaps which characterize almost all thermodynamically-consistent strain gradient plasticity (SGP) theories including higher-order dissipation. Some important results are recalled hereafter.

Proportional cyclic tension-compression and bending loading conditions were first applied to corroborate experimentally observed size effects. Good prediction of classical effects, like Hall-Petch relation, Bauschinger effects and reversible plasticity, was achieved. Furthermore, a realistic representation of the Asaro's type III kinematic hardening behavior with inflection points was obtained for the first time using 3D-DDD. This behavior corresponds to the most perfect form of plastic recovery with a first-in/last-out sequence of dislocation motion. By increasing the initial dislocation density or the grain size, it was shown that such a behavior becomes less marked and more classical Bauschinger effects take place, explaining the absence of this behavior at the macroscopic scale. Using free surface conditions, Read's "yield point"

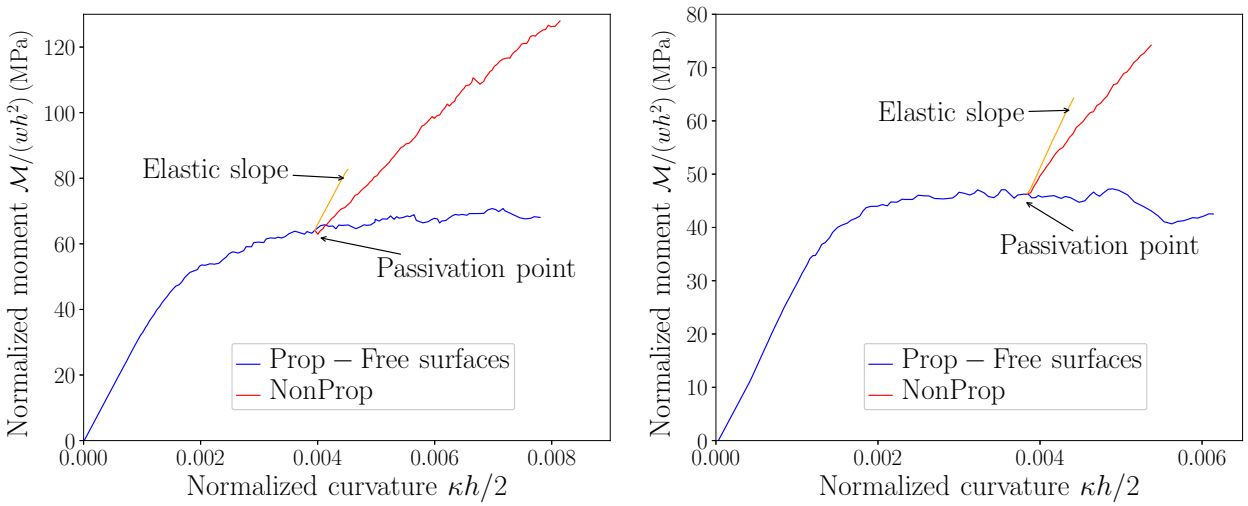

Fig. 16. Bending-passivation responses for double-slip configuration: **(a)** case with $L \times w \times h = 6 \times 2 \times 2\,\mu\text{m}^3$ and $\rho_0 = 60 \times 10^{11}\,\text{m}^{-2}$ with $L_{\text{FRs}} \in [\frac{d}{4}; \frac{d}{3}]$; **(b)** case with $L \times w \times h = 9 \times 3 \times 3\,\mu\text{m}^3$ and $\rho_0 = 100 \times 10^{11}\,\text{m}^{-2}$ with $L_{\text{FRs}} \in [\frac{3d}{8}; \frac{d}{2}]$.

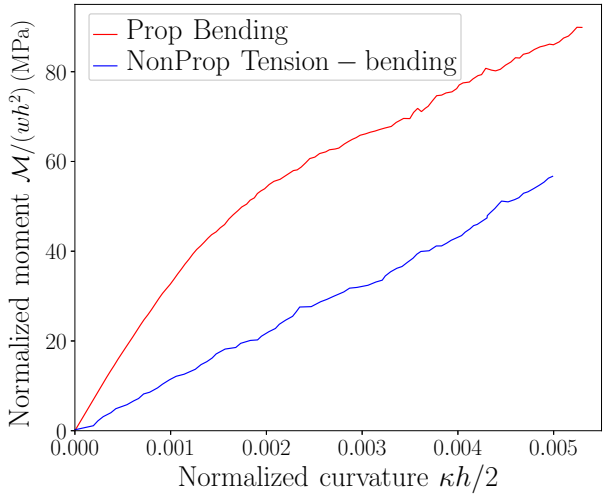

Fig. 17. Comparison between proportional bending and bending after tension.

phenomenon, which corresponds to softening-like effect in the bending curve of thin foils, was also investigated. The obtained results confirm the 2D analytical analysis of Read [73] for a material for which the stress required to move dislocations is substantially less than the stress required to activate dislocations. Overall, the results obtained using free and passivated surfaces in proportional loading conditions are in good agreement with existing experimental observations, showing the strong capabilities of 3D-DDD to accurately reproduce challenging size effects. It was then applied to investigate the occurrence of elastic gaps under non-proportional loading conditions.

Non-proportional tension-compression-passivation conditions are first considered. These conditions consist in applying tension loading with free grain surfaces until a certain level in the plastic range, then passivating the surfaces and continuing the loading cycle. It was found that no elastic gap occurs at the occurrence of the non-proportional loading source (passivation of the surfaces). The latter source only increases the plastic slope without interpreting the plastic flow. As shown by Fleck et al. [24], classical non-incremental SGP models including higher-order dissipation yield an elastic gap at the occurrence of passivation. A modified non-incremental SGP model allowing for avoiding elastic gaps under this type of loading, which generates no gradient effects before the occurrence of the non-proportional loading source, has been proposed in [13]. However, this model does not allow for avoiding elastic gaps under any non-proportional loading conditions. For example, applying non-proportional bending-passivation, the proposed model still predicts an elastic gap at the occurrence of passivation. To investigate the existence of elastic gaps under this type of loading conditions, 3D-DDD simulations implying non-proportional bending conditions were performed. As for the case of non-proportional tension-compression-passivation, no elastic gap is obtained at the occurrence of the non-proportional loading source.

Based on the current understanding of small scale plasticity mechanisms and with the demonstrated 3D-DDD capabilities to reproduce challenging size effects, the obtained results suggest that the phenomenon of elastic gaps may be not physical. Indeed, no trace of this phenomenon has been observed in all the 3D-DDD simulations under non-proportional loading conditions, which typically yield such a phenomenon when using classical Gurtin-type SGP models including higher-order dissipation. Due to the divisive nature of the issue of elastic gaps in the SGP community, experimental validation of these findings proves necessary. This challenging task will be treated in a future work. Conclusions of the present work questions the ability of classical non-incremental SGP approaches to model higher-order dissipation. Indeed, the only way for these models to avoid elastic gaps is to ignore higher-order dissipation. To the authors knowledge, there exist only two SGP models, proposed by Panteghini et al. [12] and Jebahi and Forest [15], allowing for systematically avoiding elastic gaps while considering thermodynamically-consistent higher-order dissipation. However, these models substantially deviate from classical non-incremental SGP approaches. Findings of the present paper concerning the nonexistence of elastic gaps would underscore the relevance of such models and their principle based on the kinematic decomposition of the strain gradients into recoverable and unrecoverable parts.

Acknowledgments

The authors acknowledge the financial support of the French National Research Agency (ANR) under reference ANR-20-CE08-0010 (SGP-GAPS project https://www.sgpgaps.fr/) .

Appendix A. Cyclic tension-compression with relaxed initial dislocation network

Fig. A.18 presents a comparison between tension-compression results in $\mathbf{z} = [001]$ direction obtained using $< 100 >$ oriented grains prepared with random Frank-Read sources (FRs) and the relaxation procedure of Zhou et al. [31]. Although showing some differences from a quantitative point of view, the results are qualitatively similar and lead to the same conclusions about size and non-linear kinematic hardening effects.

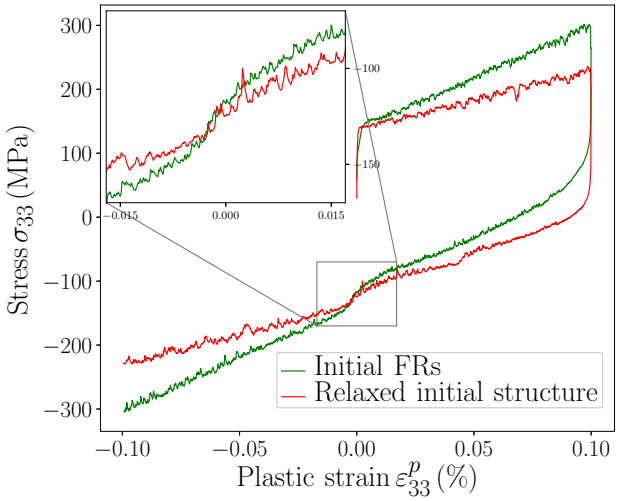

Fig. A.18. Comparison between two methods used to prepare 3D-DDD samples: random Frank-Read sources (FRs) versus relaxation procedure [31] for tension-compression, $\rho_0 = 5 \times 10^{11}\ \mathrm{m}^{-2}$.

Tab. B.4. Schmid factors associated with single-slip configuration: loading direction $\mathbf{z} = [41\bar{3}]$.

Slip system	B4	D4	D1	C1	B5	C5	D6	A6	A2	B2	C3	A3
$m_s^{\mathbf{z}=[41\bar{3}]}$	-0.22	0.	0.	0.25	0.09	-0.38	0.	**-0.47**	-0.38	-0.13	-0.13	0.09

Appendix B. Effect of the cross-slip in tension-compression

Cross-slip effects are investigated using a grain with orientation ($\mathbf{x} = [\bar{1}1\bar{1}]$, $\mathbf{y} = [275]$, $\mathbf{z} = [41\bar{3}]$) subjected to tension-compression loading in $\mathbf{z} = [41\bar{3}]$ direction. There is only one dominating slip system for this configuration (Tab. B.4), fostering cross-slipping from other slip systems to this one. Fig. B.19 compares the tension-compression results obtained with and without cross-slipping. Qualitatively, no significant differences are observed. Using non-proportional conditions, no elastic gaps are obtained for both cases.

Appendix C. Cycle bending in multi-slip configuration

Cycle bending is applied on a grain with orientation $< 100 >$ (multi-slip case) and its response is shown in Fig. C.20. With passivated surface conditions, Bauschinger effect with reversible plasticity are stronger than with free surface conditions. Asaro's type III kinematic hardening is still observed.

References

[1] N J Petch. The cleavage strength of polycrystals. *J. Iron Steel Institute*, 174:25–28, 1953.

[2] E. O. Hall. The deformation and ageing of mild steel: III discussion of results. *Proceedings of the Physical Society. Section B*, 64:747–753, 1951.

[3] N. Hansen. The effect of grain size and strain on the tensile flow stress of aluminium at room temperature. *Acta Metallurgica*, 25(8):863–869, 1977.

[4] N. A. Fleck, G. M. Muller, M. F. Ashby, and J. W. Hutchinson. Strain gradient plasticity: Theory and experiment. *Acta Metallurgica Et Materialia*, 42:475–487, 1994.

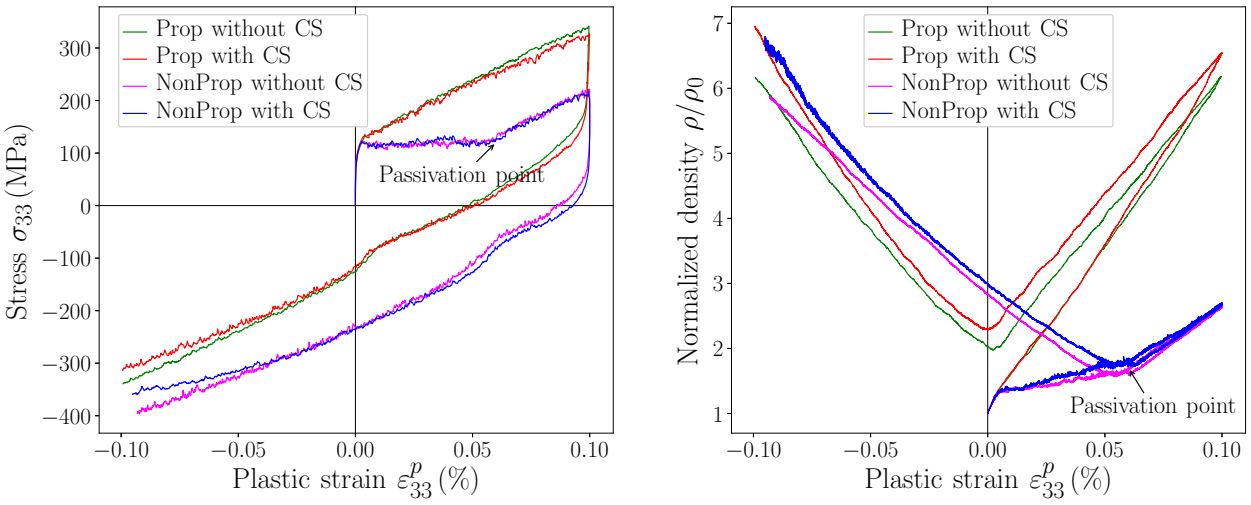

Fig. B.19. Cross-slip (CS) effects: **(a)** macroscopic tension-compression response; **(b)** evolution of the normalized density.

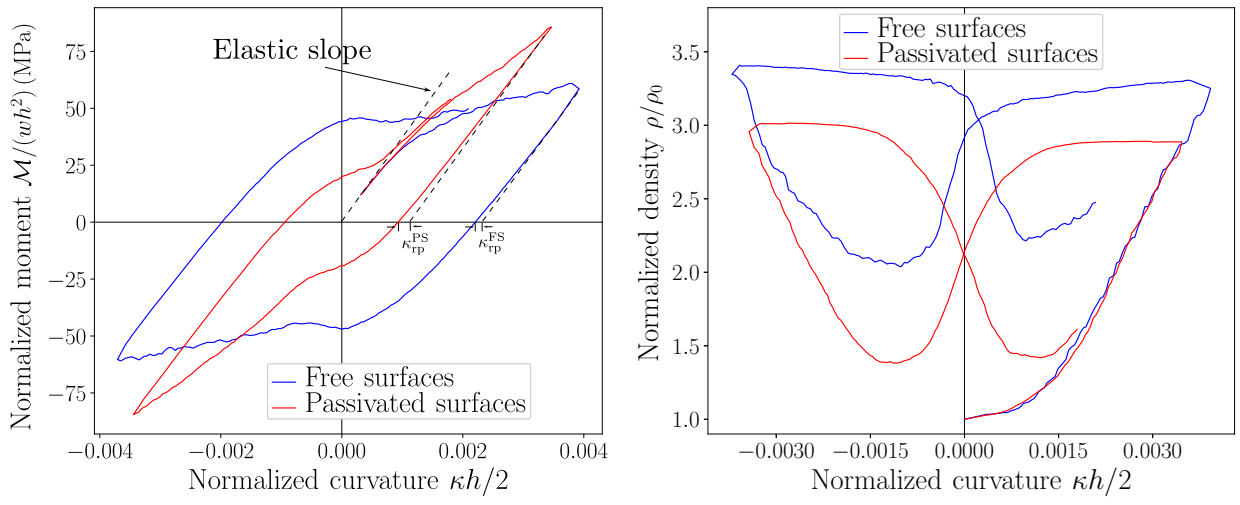

Fig. C.20. Multi-slip case, $\rho_0 = 60 \times 10^{11}\,\mathrm{m}^{-2}$ and $L \times w \times h = 9 \times 3 \times 3\,\mu\mathrm{m}^3$: **(a)** moment-curvature ($\kappa_{\mathrm{rp}}^{\mathrm{FS}}$ and $\kappa_{\mathrm{rp}}^{\mathrm{PS}}$ are respectively the recoverable plastic curvature with free and passivated surface conditions); **(b)** evolution of the normalized density.

[5] J. S. Stölken and A. G. Evans. A microbend test method for measuring the plasticity length scale. *Acta Materialia*, 46:5109–5115, 1998.

[6] C. F. O. Dahlberg, Y. Saito, M. S. Öztop, and J. W. Kysar. Geometrically necessary dislocation density measurements at a grain boundary due to wedge indentation into an aluminum bicrystal. *Journal of the Mechanics and Physics of Solids*, 105:131–149, 2017.

[7] E.C. Aifantis. On the microstructural origin of certain inelastic models. *Journal of Engineering Materials and Technology*, 106:326–330, 1984.

[8] M E Gurtin, L Anand, and S P Lele. Gradient single-crystal plasticity with free energy dependent on dislocation densities. *Journal of the Mechanics and Physics of Solids*, 55:1853–1878, 2007.

[9] John W. Hutchinson. Generalizing J2 flow theory: Fundamental issues in strain gradient plasticity. *Acta Mechanica Sinica/Lixue Xuebao*, 28:1078–1086, 2012.

[10] Lorenzo Bardella and Andrea Panteghini. Modelling the torsion of thin metal wires by distortion gradient plasticity. *Journal of the Mechanics and Physics of Solids*, 78:467–492, 2015.

[11] Emilio Martínez-Pañeda, Christian F. Niordson, and Lorenzo Bardella. A finite element framework for distortion gradient plasticity with applications to bending of thin foils. *International Journal of Solids and Structures*, 96:288–299, 2016.

[12] Andrea Panteghini, Lorenzo Bardella, and Christian F. Niordson. A potential for higher-order phenomenological strain gradient plasticity to predict reliable response under non-proportional loading. *Proceedings of the Royal Society A: Mathematical, Physical and Engineering Sciences*, 475:20190258, 2019.

[13] Mohamed Jebahi, Lei Cai, and Farid Abed-Meraim. Strain gradient crystal plasticity model based on generalized non-quadratic defect energy and uncoupled dissipation. *International Journal of Plasticity*, 126:102617, 2020.

[14] Mohamed Jebahi and Samuel Forest. Scalar-based strain gradient plasticity theory to model size-dependent kinematic hardening effects. *Continuum Mechanics and Thermodynamics*, 33:1223–1245, 2021.

[15] Mohamed Jebahi and Samuel Forest. An alternative way to describe thermodynamically-consistent higher-order dissipation within strain gradient plasticity. *Journal of the Mechanics and Physics of Solids*, 170:105103, 2023.

[16] N. A. Fleck and J. W. Hutchinson. A reformulation of strain gradient plasticity. *Journal of the Mechanics and Physics of Solids*, 49:2245–2271, 2001.

[17] Peter Gudmundson. A unified treatment of strain gradient plasticity. *Journal of the Mechanics and Physics of Solids*, 52:1379–1406, 2004.

[18] M. E. Gurtin and L. Anand. Thermodynamics applied to gradient theories involving the accumulated plastic strain: The theories of Aifantis and Fleck and Hutchinson and their generalization. *Journal of the Mechanics and Physics of Solids*, 57:405–421, 2009.

[19] N. A. Fleck, J. W. Hutchinson, and J. R. Willis. Guidelines for constructing strain gradient plasticity theories. *Journal of Applied Mechanics, Transactions ASME*, 82:1–10, 2015.

[20] C. Nellemann, C. F. Niordson, and K. L. Nielsen. An incremental flow theory for crystal plasticity incorporating strain gradient effects. *International Journal of Solids and Structures*, 110-111:239–250, 2017.

[21] N. A. Fleck and J. R. Willis. A mathematical basis for strain-gradient plasticity theory. Part I: Scalar plastic multiplier. *Journal of the Mechanics and Physics of Solids*, 57:161–177, 2009.

[22] George Z. Voyiadjis and Babur Deliktas. Mechanics of strain gradient plasticity with particular reference to decomposition of the state variables into energetic and dissipative components. *International Journal of Engineering Science*, 47:1405–1423, 2009.

[23] Lei Cai, Mohamed Jebahi, and Farid Abed-Meraim. Strain Localization Modes within Single Crystals Using Finite Deformation Strain Gradient Crystal Plasticity. *Crystals*, 11:1235, oct 2021.

[24] N. A. Fleck, J. W. Hutchinson, and J. R. Willis. Strain gradient plasticity under non-proportional loading. *Proceedings of the Royal Society A: Mathematical, Physical and Engineering Sciences*, 470, 2014.

[25] M. Fivel, M. Verdier, and G. Canova. 3D simulation of a nanoindentation test at a mesoscopic scale. *Materials Science and Engineering A*, 234-236:923–926, 1997.

[26] Julien Chaussidon, Christian Robertson, David Rodney, and Marc Fivel. Dislocation dynamics simulations of plasticity in Fe laths at low temperature. *Acta Materialia*, 56:5466–5476, 2008.

[27] Fanshi Meng, Emilie Ferrié, Christophe Déprés, and Marc Fivel. 3D discrete dislocation dynamic investigations of persistent slip band formation in FCC metals under cyclical deformation. *International Journal of Fatigue*, 149, 2021.

[28] S. A. El-Naaman, K. L. Nielsen, and C. F. Niordson. An investigation of back stress formulations under cyclic loading. *Mechanics of Materials*, 130:76–87, 2019.

[29] Jaafar A. El-Awady. Unravelling the physics of size-dependent dislocation-mediated plasticity. *Nature Communications*, 6:1–9, 2015.

[30] Ill Ryu, J. D. Gravell, Wei Cai, William D. Nix, and Huajian Gao. Intrinsic size dependent plasticity in BCC micro-pillars under uniaxial tension and pure torsion. *Extreme Mechanics Letters*, 40:100901, 2020.

[31] Caizhi Zhou, S. Bulent Biner, and Richard LeSar. Discrete dislocation dynamics simulations of plasticity at small scales. *Acta Materialia*, 58:1565–1577, 2010.

[32] Ill Ryu, Wei Cai, William D. Nix, and Huajian Gao. Stochastic behaviors in plastic deformation of face-centered cubic micropillars governed by surface nucleation and truncated source operation. *Acta Materialia*, 95:176–183, 2015.

[33] Ahmed M. Hussein, Satish I. Rao, Michael D. Uchic, Dennis M. Dimiduk, and Jaafar A. El-Awady. Microstructurally based cross-slip mechanisms and their effects on dislocation microstructure evolution in fcc crystals. *Acta Materialia*, 85:180–190, 2015.

[34] H. H.M. Cleveringa, E. Van Der Giessen, and A. Needleman. Discrete dislocation analysis of bending. *International journal of plasticity*, 15:837–868, 1999.

[35] D. Kiener, C. Motz, W. Grosinger, D. Weygand, and R. Pippan. Cyclic response of copper single crystal micro-beams. *Scripta Materialia*, 63:500–503, 2010.

[36] Haidong Fan, Qingyuan Wang, and M. Kashif Khan. Cyclic bending response of single-and polycrystalline thin films: Two dimensional discrete dislocation dynamics. *Applied Mechanics and Materials*, 275-277:132–137, 2013.

[37] C. Motz, D. Weygand, J. Senger, and P. Gumbsch. Micro-bending tests: A comparison between three-dimensional discrete dislocation dynamics simulations and experiments. *Acta Materialia*, 56:1942–1955, 2008.

[38] C. Motz and D. J. Dunstan. Observation of the critical thickness phenomenon in dislocation dynamics simulation of microbeam bending. *Acta Materialia*, 60:1603–1609, 2012.

[39] Christopher R. Weinberger and Wei Cai. Plasticity of metal wires in torsion: Molecular dynamics and dislocation dynamics simulations. *Journal of the Mechanics and Physics of Solids*, 58:1011–1025, 2010.

[40] Dabiao Liu, Yuming He, D J Dunstan, Bo Zhang, Zhipeng Gan, Peng Hu, and Huaming Ding. Anomalous Plasticity in the Cyclic Torsion of Micron Scale Metallic Wires. *Physical Review Letters*, 110:244301, 2013.

[41] Eralp Demir, Franz Roters, and Dierk Raabe. Bending of single crystal microcantilever beams of cube orientation: Finite element model and experiments. *Journal of the Mechanics and Physics of Solids*, 58:1599–1612, 2010.

[42] C. Kirchlechner, W. Grosinger, M. W. Kapp, P. J. Imrich, J. S. Micha, O. Ulrich, J. Keckes, G. Dehm, and C. Motz. Investigation of reversible plasticity in a micron-sized, single crystalline copper bending beam by X-ray μlaue diffraction. *Philosophical Magazine*, 92:3231–3242, 2012.

[43] C Motz, T Schöberl, and R Pippan. Mechanical properties of micro-sized copper bending beams machined by the focused ion beam technique. *Acta Materialia*, 53:4269–4279, 2005.

[44] Caizhi Zhou and Richard Lesar. Dislocation dynamics simulations of the Bauschinger effect in metallic thin films. *Computational Materials Science*, 54:350–355, 2012.

[45] R J Asaro. Elastic-plastic memory and kinematic-type hardening. *Acta Metallurgica*, 23:1255–1265, 1975.

[46] N. Ohno and D. Okumura. Higher-order stress and grain size effects due to self–energy of geometrically necessary dislocations. *Journal of the Mechanics and Physics of Solids*, 55:1879–1898, 2007.

[47] S. Forest. Questioning size effects as predicted by strain gradient plasticity. *Journal of the Mechanical Behavior of Materials*, 22:101–110, 2013.

[48] S. Forest and N. Guéninchault. Inspection of free energy functions in gradient crystal plasticity. *Acta Mechanica Sinica*, 29:763–772, 2013.

[49] Stephan Wulfinghoff, Samuel Forest, and Thomas Böhlke. Strain gradient plasticity modeling of the cyclic behavior of laminate microstructures. *Journal of the Mechanics and Physics of Solids*, 79:1–20, 2015.

[50] Chuantao Hou, Zhenhuan Li, Minsheng Huang, and Chaojun Ouyang. Discrete dislocation plasticity analysis of single crystalline thin beam under combined cyclic tension and bending. *Acta Materialia*, 56:1435–1446, 2008.

[51] Jamie D. Gravell and Ill Ryu. Latent hardening/softening behavior in tension and torsion combined loadings of single crystal FCC micropillars. *Acta Materialia*, 190:58–69, 2020.

[52] Y. Xiang and J. J. Vlassak. Bauschinger and size effects in thin-film plasticity. *Acta Materialia*, 54:5449–5460, 2006.

[53] Yuyang Xie, Jian Lei, Fenfei Hua, Jianhui Hu, Dabiao Liu, and Yuming He. Size and passivation effects in the torsion of thin metallic wires. *Acta Mechanica Sinica*, 39(2), 2023.

[54] M Fivel, T J Gosling, and G R Canova. Implementing image stresses in a 3D dislocation simulation. *Modelling and Simulation in Materials Science and Engineering*, 4:581–596, 1996.

[55] M. Verdier, M. Fivel, and I. Groma. Mesoscopic scale simulation of dislocation dynamics in fcc metals: Principles and applications. *Modelling and Simulation in Materials Science and Engineering*, 6:755–770, 1998.

[56] Marc Fivel and Christophe Déprés. An easy implementation of displacement calculations in 3D discrete dislocation dynamics codes. *Philosophical Magazine*, 94:3206–3214, 2014.

[57] M. Peach and J. S. Koehler. The Forces Exerted on Dislocations and the Stress Fields Produced by Them. *Physical Review*, 80:436–439, 1950.

[58] Wei Cai, Athanasios Arsenlis, Christopher R. Weinberger, and Vasily V. Bulatov. A non-singular continuum theory of dislocations. *Journal of the Mechanics and Physics of Solids*, 54:561–587, 2006.

[59] C. Déprés, C. F. Robertson, and M. C. Fivel. Low-strain fatigue in 316L steel surface grains: A three dimension discrete dislocation dynamics modelling of the early cycles. Part 2: Persistent slip markings and micro-crack nucleation. *Philosophical Magazine*, 86:79–97, 2006.

[60] Jaafar A. El-Awady, Michael D. Uchic, Paul A. Shade, Sang Lan Kim, Satish I. Rao, Dennis M. Dimiduk, and Christopher Woodward. Pre-straining effects on the power-law scaling of size-dependent strengthening in Ni single crystals. *Scripta Materialia*, 68:207–210, 2013.

[61] Songjiang Lu, Qianhua Kan, Michael Zaiser, Zhenhuan Li, Guozheng Kang, and Xu Zhang. Size-dependent yield stress in ultrafine-grained polycrystals: A multiscale discrete dislocation dynamics study. *International Journal of Plasticity*, 149:103183, 2022.

[62] Y. N. Cui, P. Lin, Z. L. Liu, and Z. Zhuang. Theoretical and numerical investigations of single arm dislocation source controlled plastic flow in FCC micropillars. *International Journal of Plasticity*, 55:279–292, 2014.

[63] Maoyuan Jiang, Ghiath Monnet, and Benoit Devincre. On the origin of the Hall-Petch law: A 3D-dislocation dynamics simulation investigation. *Acta Materialia*, 209:116783, 2021.

[64] M. Longsworth and M. Fivel. Investigating the cross-slip rate in face-centered cubic metals using an atomistic-based cross-slip model in dislocation dynamics simulations. *Journal of the Mechanics and Physics of Solids*, 153:104449, 2021.

[65] Haidong Fan, Qingyuan Wang, Jaafar A. El-Awady, Dierk Raabe, and Michael Zaiser. Strain rate dependency of dislocation plasticity. *Nature Communications*, 12:1–12, 2021.

[66] Maoyuan Jiang, Benoit Devincre, and Ghiath Monnet. Effects of the grain size and shape on the flow stress: A dislocation dynamics study. *International Journal of Plasticity*, 113:111–124, 2019.

[67] R. Taillard and A. Pineau. Room temperature tensile properties of Fe-19wt.precipitation hardened by the intermetallic compound NiAl. *Materials Science and Engineering*, 56:219–231, 1982.

[68] Philip Croné, Peter Gudmundson, and Jonas Faleskog. Strain gradient plasticity modelling of cyclic loading in dispersion hardened materials. *European Journal of Mechanics, A/Solids*, 96:104741, 2022.

[69] Z. C. Cordero, B. E. Knight, and C. A. Schuh. Six decades of the Hall-Petch effect - a survey of grain-size strengthening studies on pure metals. *International Materials Reviews*, 61:495–512, 2016.

[70] S. Yefimov, E. Van Der Giessen, and I. Groma. Bending of a single crystal: Discrete dislocation and nonlocal crystal plasticity simulations. *Modelling and Simulation in Materials Science and Engineering*, 12:1069–1086, 2004.

[71] Severin Schmitt, Markus Stricker, Peter Gumbsch, and Katrin Schulz. A mechanism-based homogenization of a dislocation source model for bending. *Acta Materialia*, 164:663–672, 2019.

[72] D. M. Barnett. The displacement field of a triangular dislocation loop. *Philosophical Magazine A: Physics of Condensed Matter, Structure, Defects and Mechanical Properties*, 51:383–387, 1985.

[73] W.T Read. Dislocation theory of plastic bending. *Acta Metallurgica*, 5:83–88, 1957.